Quaternary Science Reviews 201 (2018) 429–445

Contents lists available at ScienceDirect

Quaternary Science Reviews

journal homepage: www.elsevier.com/locate/quascirev

Variations in Western Pacific Warm Pool surface and thermocline conditions over the past 110,000 years: Forcing mechanisms and implications for the glacial Walker circulation

Martina Hollstein [a, *], Mahyar Mohtadi [a], Yair Rosenthal [b], Matthias Prange [a], Delia W. Oppo [c], Gema Martínez Méndez [a], Kazuyo Tachikawa [d], Paola Moffa Sanchez [e], Stephan Steinke [f], Dierk Hebbeln [a]

[a] MARUM – Center for Marine Environmental Sciences, University of Bremen, Bremen, Germany
[b] Department of Marine and Coastal Sciences, Rutgers, State University of New Jersey, USA
[c] Department of Geology and Geophysics, Woods Hole Oceanographic Institution, Massachusetts, USA
[d] Aix Marseille University, CNRS, IRD, INRA, Coll France, CEREGE, Aix-en-Provence, France
[e] School of Earth and Ocean Sciences, Cardiff University, Cardiff, UK
[f] Department of Geological Oceanography and State Key Laboratory of Marine Environmental Science (MEL), Xiamen University, Xiamen, China

ARTICLE INFO

Article history:
Received 17 August 2018
Received in revised form
16 October 2018
Accepted 19 October 2018

ABSTRACT

Surface and thermocline conditions of the Western Pacific Warm Pool (WPWP) reflect changes in regional and basin scale ocean and atmosphere circulations and in turn may affect climate globally. Previous studies suggest that a range of factors influences the WPWP on different timescales, however the precise forcings and mechanisms are unclear. Combining surface and thermocline records from sediment cores offshore Papua New Guinea we explore the influence of local and remote processes on the WPWP in response to astronomical forcing and changing glacial-interglacial boundary conditions over the past 110 kyr. We find that thermocline temperatures change with variations in Earth's obliquity with higher temperatures coinciding with high obliquity, which is attributed to variations in subduction and advection of the South Pacific Tropical Water. In contrast, rainfall variations associated with meridional migrations of the Intertropical Convergence Zone are primarily driven by changes in insolation due to precession. Records of bulk sedimentary Ti/Ca and foraminiferal Nd/Ca indicate an additional influence of obliquity, which, however, cannot unambiguously be related to changes in precipitation. Finally, our results suggest a thermocline deepening during the Last Glacial Maximum (LGM). A compilation of available proxy records illustrates a dipole-like pattern of LGM thermocline depth anomalies with a shoaling (deepening) in the northern (southern) WPWP. A comparison of the proxy compilation with an ensemble of Paleoclimate Model Intercomparison Project (PMIP) climate model simulations reveals that the spatial pattern of LGM thermocline depth anomalies is mainly attributable to a contraction of the Pacific Walker circulation on its western side.

1. Introduction

The Western Pacific Warm Pool (WPWP) is a critical element within the global climate and ocean system. It is a major source of heat and moisture to the global atmosphere [e.g. Gagan et al., 2004] with far-reaching climate impacts. Its present climate is linked to the Australasian monsoon system and the seasonally migrating Intertropical Convergence Zone (ITCZ), and other large-scale climate phenomena, such as the El Niño–Southern Oscillation (ENSO), which affects climate worldwide. In addition, the equatorial current system of the WPWP links the equatorial Pacific Ocean to the Indonesian Throughflow (ITF), which is an important component of the global ocean circulation [e.g. Gordon, 1986].

Due to its significant influence on global climate and ocean conditions, many recent studies have focused on the reconstruction of past WPWP climate and ocean dynamics [e.g. Dang et al., 2012; DiNezio et al., 2011; Lea et al., 2000; Leech et al., 2013; Sagawa et al.,

* Corresponding author.
E-mail address: mhollstein@marum.de (M. Hollstein).

https://doi.org/10.1016/j.quascirev.2018.10.030
0277-3791/

2012]. Long-term variations in climate and ocean dynamics have been attributed to a range of factors, such as variations in the state of ENSO and the Walker circulation [e.g. Bolliet et al., 2011; Sagawa et al., 2012], changes in the Australasian monsoon system, associated migrations of the ITCZ, and the Hadley circulation [e.g. Dang et al., 2012; Tachikawa et al., 2011], and a possible remote effect of southern hemisphere mid and high latitudes [e.g. Rosenthal et al., 2013] in response to astronomical forcing and changing glacial-interglacial boundary conditions.

Precession controls the seasonal distribution of the incoming solar radiation in the northern and southern hemisphere. It therefore has a strong influence on the latitudinal position of the ITCZ and the Australasian monsoon and may affect the WPWP hydroclimate through interhemispheric alternating rainfall variations with high (low) precipitation in the southern hemisphere when precession is high (low) [e.g. Merlis et al., 2013]. Accordingly, proxy records indicated that the rainfall around Papua New Guinea (PNG) is stronger (weaker) when precession is high (low) [e.g. Dang et al., 2015; Tachikawa et al., 2011]. Records from Indonesia and numerical simulations suggest that the WPWP hydroclimate is additionally controlled by complex changes in the Walker circulation that might be directly tied to insolation or to glacial–interglacial boundary conditions [Cheng et al., 2012 and references therein].

Obliquity (the Earth's axial tilt) has only a very small influence on low-latitude insolation, yet various records from the tropical Pacific exhibit a strong 41-kyr signal [e.g. Beaufort et al., 2001; de Garidel-Thoron et al., 2005; Lea et al., 2000]. Numerical studies also indicate a direct influence of obliquity on tropical Pacific climate via reorganizations in the Hadley circulation [Bosmans et al., 2015; Mantsis et al., 2011; Mantsis et al., 2014] consistent with evidence from offshore PNG, which indicates suppressed rainfall over PNG during high obliquity [Liu et al., 2015]. In addition, many Holocene Mg/Ca-derived surface and thermocline temperature records from the tropical Pacific and Indonesian Seas show a cooling trend, which has been related to the remote influence of insolation changes at mid- and high-latitudes [e.g. Rosenthal et al., 2013; Rosenthal et al., 2017].

In addition to the direct influence of insolation, varying glacial-interglacial boundary conditions such as atmospheric CO_2 concentrations, extent of ice sheets in high latitudes and sea level additionally control the climate and ocean conditions in the WPWP, probably affecting both, the Hadley [e.g. Leech et al., 2013], and Walker circulation [e.g. DiNezio et al., 2011] and/or the state and activity of ENSO [e.g. Andreasen and Ravelo, 1997]. However, hitherto available studies provide conflicting evidence, for instance either indicating a weaker Walker circulation and/or more El Niño-like conditions [e.g. Koutavas et al., 2002; Prange et al., 2010; Sadekov et al., 2013; Sagawa et al., 2012] or a stronger Walker circulation and/or more La Niña-like conditions [e.g. Andreasen and Ravelo, 1997; Ford et al., 2015; Zhu et al., 2017] during the Last Glacial Maximum (LGM).

Available paleoceanographic reconstructions mostly focus on the LGM, the deglaciation and/or the Holocene, and thus provide a limited view on the driving forces and mechanisms that control climate and ocean conditions in the WPWP, especially astronomical forcing, which is best assessed from a longer-term perspective. Besides, many inferences are based solely on sea surface records, whereas thermocline reconstructions are sparse. Thermocline reconstructions may help to improve our understanding of the WPWP ocean and climate dynamics and their global reach for the following reasons: First, the thermocline structure reflects overlying winds and climate dynamics and indeed the depth and state of the thermocline is closely linked to the prevailing climate conditions. Modern observations show that the state of ENSO and associated variations in the Pacific Walker circulation affect the depth and tilt of the thermocline, with a thermocline shoaling in the WPWP during El Niño, when the Pacific Walker circulation is relaxed and a thermocline deepening during La Niña, when the Pacific Walker circulation is relatively strong. Records of thermocline depth may therefore be used to draw clues on past variations in the state of the Pacific Ocean and the Walker circulation. Second, thermocline waters offshore PNG originate in the extratropical South Pacific Ocean (see study area for more details). Thermocline reconstructions therefore provide the opportunity to improve our understanding of the links between the WPWP and extratropical climate variability and their influence on the equatorial Pacific climate. Finally, WPWP thermocline waters feed the ITF. Numerous studies focus on the evolution of the ITF [e.g. Ding et al., 2013; Xu et al., 2008], but the robustness of their interpretations is limited due to the weak understanding of variations in the WPWP thermocline waters supplying the ITF.

Here, we use high-resolution surface water and thermocline records from offshore PNG (Fig. 1) spanning the past 110 kyr to assess the influence of both, local factors and remote processes on the WPWP in response to astronomical forcing and changing glacial-interglacial boundary conditions. To this end, we combine new and published Mg/Ca and $\delta^{18}O$ data of the planktic foraminifera *Globigerinoides ruber* and *Pulleniatina obliquiloculata* from core GeoB17419-1 and the nearby core MD05-2920 [Tachikawa et al., 2014] and estimate the past evolution of surface and thermocline temperatures and oxygen isotope compositions of seawater ($\delta^{18}O_{SW}$). To assess past changes in precipitation above PNG we additionally use bulk sedimentary Ti/Ca and foraminiferal Nd/Ca ratios. We further calculate the difference between surface and thermocline temperatures (ΔT) to reconstruct variations in the vertical structure of the upper water column and use available Paleoclimate Model Intercomparison Project (PMIP) climate model output to infer features of the glacial tropical atmosphere circulation from reconstructed thermocline depth anomalies.

2. Study area

The GeoB 17419-1 and MD05-2920 core sites are located in the center of the WPWP offshore PNG, approximately 100–150 km offshore the Sepik River mouth. SST within the study area exceed 28 °C year-round and sea surface salinity varies around 34.0 to 34.5 psu (Figs. 1 and 2) [Carton and Giese, 2008; Locarnini et al., 2013; Zweng et al., 2013]. The mixed layer is between 50 and 100 m deep [Locarnini et al., 2013].

Today, the Australasian monsoon and connected migrations of the ITCZ affect the regional climate on a seasonal scale. During the southeast monsoon season (austral winter), southeast winds dominate and the ITCZ is located to the north of the equator. During the northwest monsoon season (austral summer) winds reverse and the ITCZ is located to the south of the equator, which leads to increased precipitation over the study area and PNG (Fig. 2a). Average seasonal variations in surface temperature and salinity are very small and within the range of 1–2 °C for temperature and below 1 psu for salinity (Fig. 2) [Carton and Giese, 2008; Locarnini et al., 2013; Zweng et al., 2013]. Seasonal variations in winds lead to only minor changes in the thermal stratification of the upper water column [Carton and Giese, 2008]. On interannual timescales, the regional climate is influenced by changes in the Walker circulation and ENSO. They affect surface and particularly thermocline ocean conditions as well as the vertical structure of the water column. El Niño (La Niña) is characterized by a weakening and eastward displacement (strengthening) of the Walker circulation, which is associated with a cooling (warming) of sub(surface) temperatures and a thermocline shoaling (deepening) at the core site (Fig. 2).

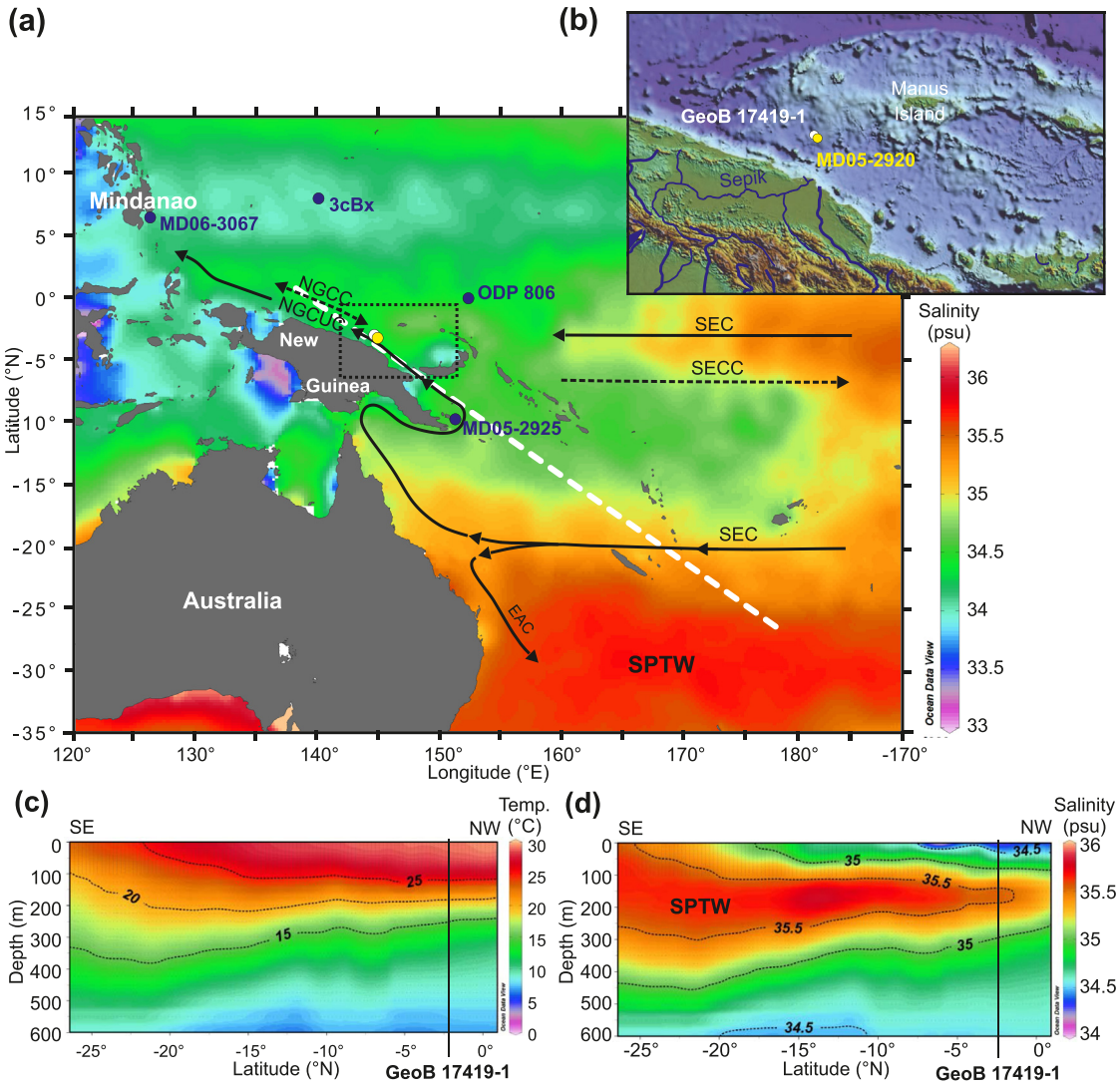

Fig. 1. (a) Mean annual sea surface salinity and surface ocean circulation within the study area. Dashed and solid arrows indicate surface and subsurface currents, respectively. SEC – South Equatorial Current, SECC – South Equatorial Counter Current, NGCC – New Guinea Coastal Current, NGCUC – New Guinea Coastal Undercurrent, EAC – East Australian Current. The black stippled rectangle denotes a close up of the study area presented in (b). The white stippled line indicates the location of the temperature and salinity sections shown in (c) and (d). (b) Bathymetric map of the study area. White and yellow dots show the positions of cores GeoB 17419-1 (this study) and MD05-2920 [Tachikawa et al., 2014]. Other records mentioned in this study are indicated by dark blue dots. (c) Temperature and (d) salinity sections along the profile indicated on the map (yellow line). Vertical black bars mark the latitude of site GeoB 17419-1. Note that the thermocline is influenced by the high salinity South Pacific Tropical Water (SPTW). Temperature and salinity data are from WOA13 [Locarnini et al., 2013; Zweng et al., 2013]. The sections were created with the Ocean Data View software [Schlitzer, 2014]. (For interpretation of the references to color in this figure legend, the reader is referred to the Web version of this article.)

Related thermocline depth anomalies in the study area are in the order of several tens of meters. For example, the 20 °C isotherm, often used as an indicator for the thermocline depth in the WPWP, varied up to 40 m in relation to ENSO between 1986 and 1998 [Harrison and Vecchi, 2001]. The interannual rainfall variability within the study area is less clear. While the gridded precipitation data by Beck et al., [2005] imply that precipitation over the catchment area of the Sepik River is modulated by ENSO and related changes in the Walker circulation with slightly drier (wetter) conditions during El Niño (La Niña) (Fig. 2), studies by Smith et al., [2013] and As-syakur et al., [2014] demonstrate that precipitation over PNG and the Bismarck Sea does not vary uniformly in response to ENSO. Consequently, salinity at the core site does not show a clear response to ENSO (Fig. 2). Overall, regional rainfall and salinity are predominantly controlled by seasonal migrations of the ITCZ, while surface and thermocline temperature and thermocline depth variations are mainly controlled by ENSO and related changes in the Walker circulation.

The thermocline waters within the study area are marked by high salinity with a maximum around 35.5 psu that characterizes the South Pacific Tropical Water (SPTW). The SPTW is produced by subduction of surface waters within the South Pacific subtropical gyre [e.g. Qu et al., 2013; Tsuchiya et al., 1989] and transported into the study area within the regional sub(surface) circulation system (Fig. 1). The (sub)surface circulation is dominated by the westward flowing South Equatorial Current (SEC) and by western boundary currents that flow equatorward along the northern east coast of Australia and New Guinea (Fig. 1). The core sites are located within the flow path of the New Guinea Coastal Current (NGCC) and the New Guinea Coastal Undercurrent (NGCUC). Driven by trade winds, the NGCC reverses seasonally flowing westward along the coast of PNG during austral winter and eastward during austral summer.

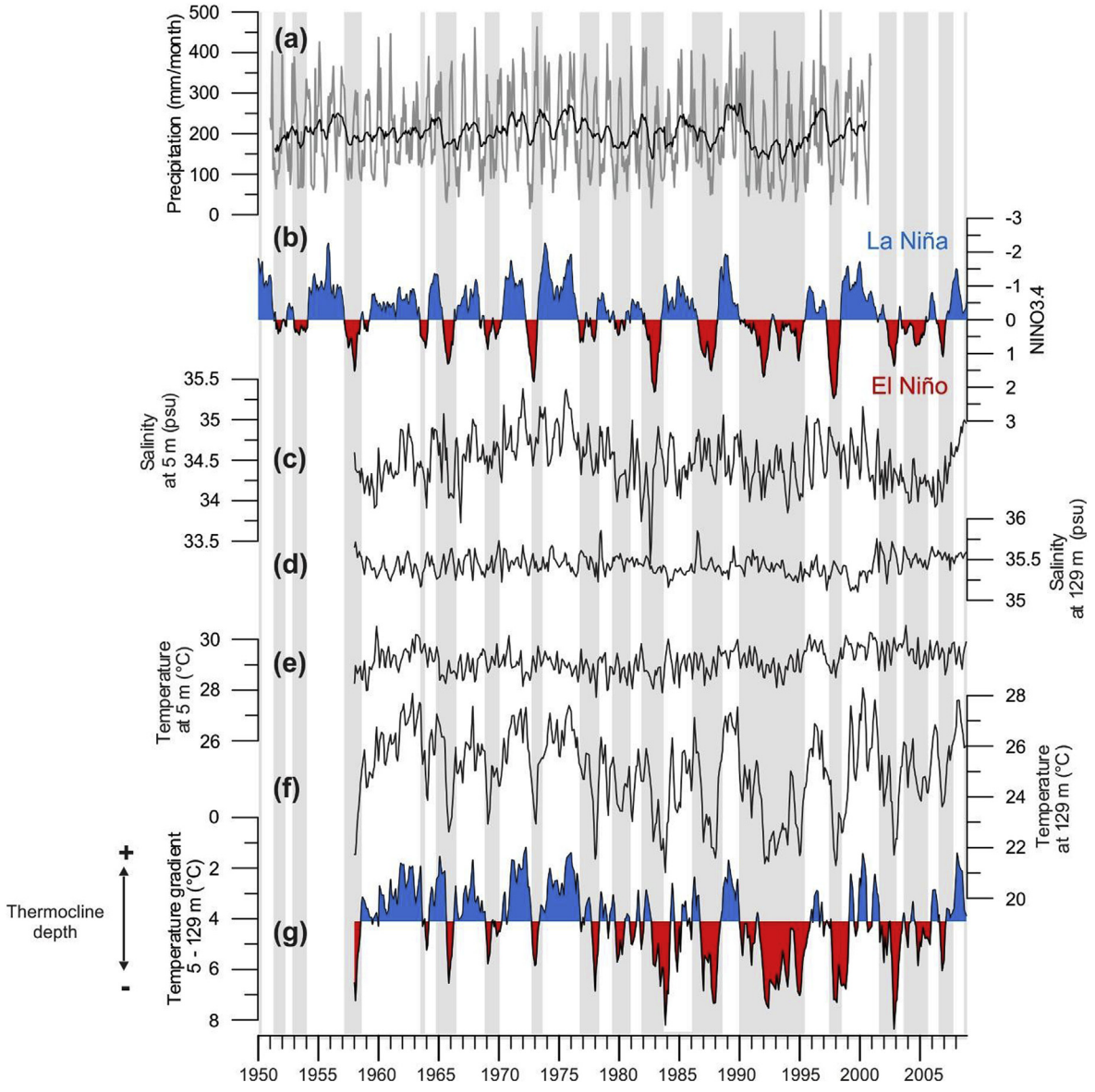

Fig. 2. Monthly climatology of the study area. (a) Monthly precipitation rate above the catchment area of the Sepik River (gray) (143.50–144.50 °E, 3.50–4.50 °S) [Beck et al., 2005] with an 11-point running mean (black). (b) Niño3.4 index (http://www.cpc.ncep.noaa.gov/data/indices/). (c, d) Surface (5 m) and thermocline (129 m) salinity and (e, f) temperature at the study site from SODA 2.1.6 at 144.25 °E and 2.25 °S [Carton and Giese, 2008]. (g) Difference between surface and subsurface temperatures used as an indicator for thermocline depth. Gray bars indicate El Niño periods. Note that rainfall and salinity variations are dominated by seasonal variations, while temperature and thermocline depth variations are mainly ENSO controlled.

The NGCUC does not reverse seasonally, but the westward flow is weaker during austral summer [e.g. Cresswell, 2000; Kuroda, 2000].

3. Material and methods

3.1. Material

Gravity core GeoB 17419-1 was retrieved during R/V SONNE expedition SO–228 offshore PNG (2.81 °S, 144.50 °E, 1883 m water depth, 914 cm length) [Mohtadi et al., 2013]. Samples for geochemical analyses were taken at 4 cm intervals. All samples were freeze dried, washed over 150 μm sieves and dried. The core site is located well above the modern position of the calcite lysocline at ~3300 m water depth [see Berger et al., 1982 and references therein]. The presence of aragonitic pteropods in many of the samples additionally indicates a good carbonate preservation.

For our study, we use the geochemical signature of *G. ruber* and *P. obliquiloculata* shells as indicator for surface and upper thermocline conditions, respectively. The choice of species is based on $\delta^{18}O$-derived calcification depth estimates for site GeoB 17419-1, which indicate that *G. ruber* calcifies within the upper 60 m of the water column (mixed layer) and *P. obliquiloculata* between 110 and 150 m water depth (upper thermocline) [Hollstein et al., 2017]. Previous studies indicate that both species calcify perennially in the study area [Kawahata et al., 2002; Yamasaki et al., 2008]. We generated new Mg/Ca and $\delta^{18}O$ records of *P. obliquiloculata* and a new $\delta^{18}O$ of *G. ruber* of core GeoB 17419-1. We then combined the surface $\delta^{18}O$ and the thermocline Mg/Ca record with the published Mg/Ca-based SST record of nearby core MD05-290 [Tachikawa et al., 2014] to estimate surface $\delta^{18}O_{SW}$ and surface-thermocline ΔT, respectively. Coherent variations of the benthic $\delta^{18}O$ and Ti/Ca

records of the GeoB 17419-1 and MD05-2920 cores provide confidence that the Mg/Ca and $\delta^{18}O$ records can be combined (supplementary information S1).

3.2. Age model

Between 6 and 414 cm core depth, the age model of GeoB 17419-1 is based on 26 accelerator mass spectrometry (AMS) ^{14}C ages, measured either on *Globigerinoides sacculifer* or on mixed *G. ruber, Globigerinoides elongatus* and *G. sacculifer* samples. The measurements were performed at the Keck Carbon Cycle Accelerator Mass Spectrometry Laboratory at the University of California, Irvine. The age-depth relation was modeled with a Bayesian approach using the software BACON R 2.2 (see supplementary information for details) [Blaauw and Christen, 2011]. Radiocarbon ages were converted to calendar ages using the Marine13 calibration curve [Reimer et al., 2013] and applying a local reservoir age correction of $\Delta R = 70 \pm 60$ yrs [McGregor et al., 2008]. The age uncertainty given as 95% confidence interval ranges between 145 and 1365 yrs. Below 414 cm the age model is based on visual correlation of benthic $\delta^{18}O$ of *Cibicides wuellerstorfi* (see section 3.4 for details on isotope measurements) to the global benthic stack LR04 [Lisiecki and Raymo, 2005]. We defined tie points at the core bottom, which is associated with the onset of Marine Isotope Stage (MIS) 5c and at maxima in $\delta^{18}O$ associated with MIS 5b and MIS 4 (Table 1, Fig. 3). Between these tie points, the chronology was inferred by linear interpolation. To extend the record of the gravity core GeoB 17419-1 to present, we use $\delta^{18}O$ and Mg/Ca values measured on the core top of the multi core (MUC) GeoB 17419-2, which was retrieved at the same location. The core top is radiocarbon dated and reflects modern ocean conditions [Hollstein et al., 2017]. All ages are given in calendar years before present (BP).

Since we combine temperature and $\delta^{18}O$ records from GeoB 17419-1 with the published SST record of MD05-2920 to calculate a surface $\delta^{18}O_{SW}$ and ΔT, tying the age models of the cores to each other is critical. We therefore revised the age model of MD05-2920. Additionally, we used Ti/Ca elemental ratios that were measured in high resolution in both cores to validate the age models. The Ti/Ca records are in good agreement. Unavoidable minor offsets between the records (generally < 1 ka) do not affect the conclusions of our study (see supplementary information S1 for further details).

3.3. X-Ray Fluorescence (XRF) core scanner analyses

Ti and Ca intensities in GeoB 17419-1 were measured with an X-Ray Fluorescence (XRF) Core Scanner at MARUM, University of Bremen. Data were collected every 2 cm down-core over a 1.2 cm^2 area with a down-core slit size of 10 mm using generator settings of 10 kV, a current of 0.02 mA, and a sampling time of 20 s directly at the split core surface of the archive half with XRF Core Scanner III (AVAATECH Serial No. 12). Prior to core scanning, the split core surface was covered with a 4 μm thin SPEXCerti Prep Ultralene1 foil to avoid contamination of the XRF measurement unit and desiccation of the sediment. The data have been acquired by a Canberra X-PIPS Silicon Drift Detector (SDD; Model SXD 15C-150-500) with 150eV X-ray resolution, the Canberra Digital Spectrum Analyzer DAS 1000 and an Oxford Instruments 100W Neptune X-ray tube with rhodium (Rh) target material. Raw data spectra were processed by the Analysis of X-ray spectra by Iterative Least square software (WIN AXIL) package from Canberra Eurisys.

Table 1
AMS-^{14}C ages and calibrated calendar ages of core GeoB 17419-1 as well as tie points used to construct the age model of GeoB 17419-1. For the radiocarbon dated part of the core weighted mean ages are given as estimated by the BACON run.

Lab-ID	Sample depth (cm)	Foraminifera species	^{14}C age ± 1σ error (years BP)	Cal. age (years BP)	95% confidence interval (years)
142706	6	*G. sacculifer*	1515 ± 20	1033	246–1117
156177	14	*G. ruber* + *G. sacculifer*	2385 ± 25	1923	1727–2115
150149	38	*G. sacculifer*	4505 ± 20	4607	4378–4810
142707	58	*G. sacculifer*	6395 ± 20	6788	6640–6931
142708	58	*G. sacculifer*	6365 ± 20	6788	6640–6931
150150	66	*G. sacculifer*	7235 ± 20	7260	6982–7568
150151	74	*G. sacculifer*	6625 ± 20	7391	7138–7711
156178	82	*G. ruber* + *G. sacculifer*	7415 ± 25	7724	7468–7956
156179	90	*G. ruber* + *G. sacculifer*	8810 ± 25	9266	9009–9525
156180	98	*G. ruber* + *G. sacculifer*	9245 ± 25	9975	9740–10193
146301	106	*G. ruber* + *G. sacculifer*	9490 ± 30	10304	10138–10448
156181	114	*G. ruber* + *G. sacculifer*	9530 ± 25	10512	10354–10688
156182	122	*G. ruber* + *G. sacculifer*	10880 ± 35	12210	11754–12583
156183	130	*G. ruber* + *G. sacculifer*	11520 ± 30	12928	12723–13143
150152	138	*G. sacculifer*	11900 ± 30	13365	13177–13553
156184	142	*G. ruber* + *G. sacculifer*	12270 ± 30	13634	13433–13850
156185	148	*G. ruber* + *G. sacculifer*	12730 ± 30	14191	13927–14564
146302	156	*G. ruber* + *G. sacculifer*	13175 ± 40	15059	14724–15315
156203	164	*G. ruber* + *G. sacculifer*	13565 ± 40	15646	15378–15905
156186	172	*G. ruber* + *G. sacculifer*	13705 ± 35	15986	15754–16194
156187	180	*G. ruber* + *G. sacculifer*	13760 ± 35	16218	16026–16421
150153	192	*G. sacculifer*	14730 ± 45	17276	16751–17682
146303	208	*G. ruber* + *G. sacculifer*	16145 ± 45	18909	18475–19210
156188	228	*G. ruber* + *G. sacculifer*	16990 ± 50	20035	19696–20343
146304	256	*G. ruber* + *G. sacculifer*	19060 ± 60	22471	22099–22757
156189	268	*G. ruber* + *G. sacculifer*	19600 ± 60	23147	22855–23470
150154	288	*G. sacculifer*	20290 ± 100	24052	23690–24409
146940	308	*G. ruber* + *G. sacculifer*	21760 ± 160	25575	25001–26051
146941	356	*G. ruber* + *G. sacculifer*	26210 ± 260	29769	28922–30561
146942	412	*G. ruber* + *G. sacculifer*	30340 ± 440	33568	32249–34563
_	748	-	–	66000	–
_	836	-	–	87000	–
_	904	-	–	110000	–

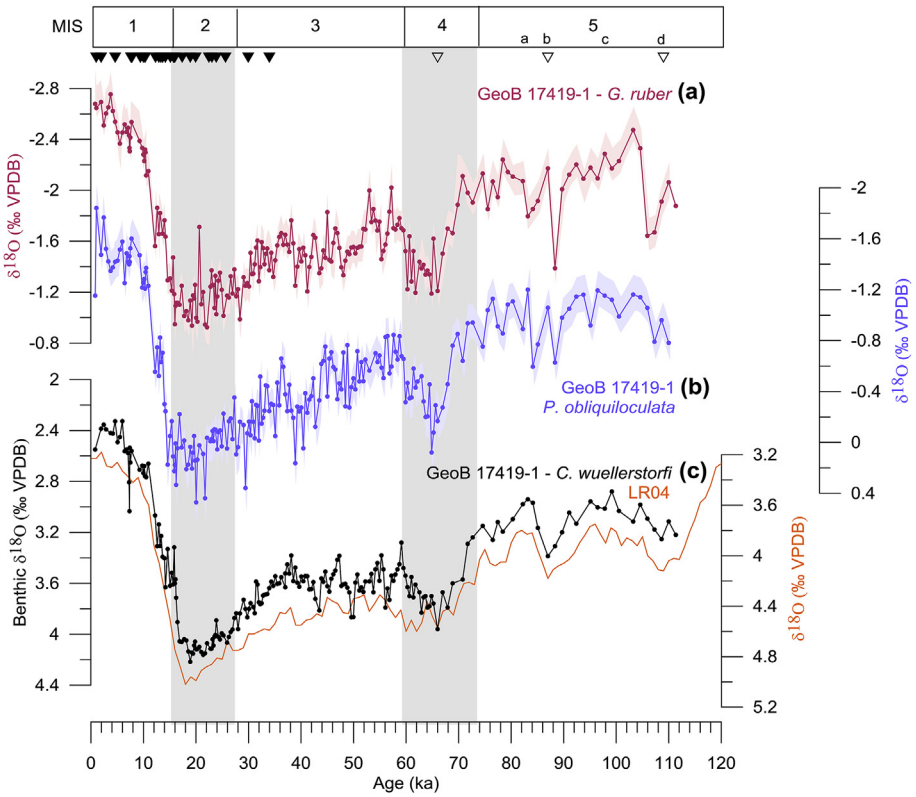

Fig. 3. Planktic and benthic $\delta^{18}O$ and age model of core GeoB 17419-1. Shell $\delta^{18}O$ of (a) *G. ruber* and (b) *P. obliquiloculata*. Shadings represent 1σ-uncertainties (see section 3.4). (c) Shell $\delta^{18}O$ of *C. wuellerstorfi* (black line) compared to the LR04 benthic $\delta^{18}O$ stack of Lisiecki and Raymo [2005] (orange line). Filled triangles indicate radiocarbon dates of GeoB 17419-1; open triangles denote tie points to LR04. Marine isotopes stages (MIS) 1–5 as dated by Sanchez Goñi and Harrison [2010] are indicated at the top. Gray bars mark glacial periods (MIS 2 and 4). (For interpretation of the references to color in this figure legend, the reader is referred to the Web version of this article.)

3.4. Stable oxygen isotope, Mg/Ca and Nd/Ca analyses

In order to establish the age model for core GeoB17419-1 we generated a $\delta^{18}O$ record on the benthic foraminifera *C. wuellerstorfi* (size fraction 250–425 μm). For reconstructing $\delta^{18}O_{SW}$ we measured $\delta^{18}O$ of the planktic foraminifera *G. ruber* (size fraction 250–355 μm) and *P. obliquiloculata* (size fraction 355–425 μm). Identification of *G. ruber* followed the species concept of Aurahs et al., [2011]. Hence, only individuals previously referred to as *G. ruber* s.s. were included.

Isotope analyses were performed at MARUM, University of Bremen on Finnigan MAT 251 mass spectrometers with Kiel I or Kiel III devices. Isotope values were calibrated against the international Vienna Pee Dee Belemnite (VPDB) standard. The internal carbonate standard is a Solnhofen Limestone, which is calibrated to the National Bureau of Standards (NBS) 19 standard. The long-term analytical precision was better than ±0.07‰. Replicate measurements on 10% of the samples indicate an average standard deviation of 0.12‰ for *G. ruber* (n = 22) and 0.14‰ for *P. obliquiloculata* (n = 22).

For Mg/Ca and Nd/Ca measurements, we used ~20 specimens of *P. obliquiloculata* per sample. Foraminifera tests were weighed to estimate a potential influence of test dissolution on the Mg/Ca records and gently crushed to open the chambers. We applied a full trace metal cleaning including a reductive step [Boyle and Keigwin, 1985] as modified by Rosenthal et al., [1997] and Rosenthal et al., [1999]. The cleaned samples were dissolved in 0.065 M HNO_3, centrifuged (10 min at 10000 rpm), and diluted with 0.5 M HNO_3. The final calcium concentration of the samples averaged 5.5 mM (between 1.0 and 9.7 mM). The samples were analyzed at Rutgers University, New Jersey using a Thermo Fisher/Finnigan Element XR sector-field inductively coupled mass spectrometer (ICP-MS). Measured ratios were blank corrected. The long term reproducibility of the data, drift and matrix effects were controlled by repeated measurements of in house consistency standards [Rosenthal et al., 1999]. The long-term precision of the instrument was about of ±1.0% and <2.5% for Mg/Ca and Nd/Ca, respectively. All Mg/Ca ratios are given in mmol/mol, Nd/Ca is reported in μmol/mol. Replicates indicate a sample reproducibility of ±0.3 mmol/mol for Mg/Ca and ±0.2 mmol/mol for Nd/Ca (n = 22). We monitored the cleaning efficacy by measuring Al/Ca, Fe/Ca and Mn/Ca alongside with Mg/Ca. None of these ratios co-varies with Mg/Ca, indicating that the Mg/Ca ratios are not affected by contaminant phases. Mg/Ca values do not correlate to shell normalized weights (Fig. S2), suggesting that shell Mg/Ca is not substantially affected by carbonate dissolution.

Mg/Ca could additionally be influenced by salinity and carbonate chemistry. Culture and core top studies disagree on the magnitude of the influence of salinity on planktic foraminiferal Mg/Ca [e.g. Arbuszewski et al., 2010; Hönisch et al., 2013; Kısakürek et al., 2008]. However, recent calibrations based on sediment traps and modern WPWP core tops provide confidence that the effect is negligible in the study area [Hollstein et al., 2017; Zhang et al., 2018]. The magnitude of seawater pH and $[CO_3^{2-}]$ effects on Mg/Ca, which could lead to an overestimation of past temperature changes [e.g. Gray et al., 2018], is uncertain. Several studies indicate that the effect is relatively small under ambient seawater conditions [Kısakürek et al., 2008; Russell et al., 2004] and further decreasing above ambient pH [Allen et al., 2016], providing confidence that the carbonate chemistry does not substantially bias our

Mg/Ca-based temperature estimates.

To convert the Mg/Ca ratios of *P. obliquiloculata* to temperature, we applied the species-specific equation established for the modern WPWP by Hollstein et al., [2017]:

$$Mg/Ca = 0.21 \exp 0.097^{*}T$$

For the surface, we used the published Mg/Ca-based temperature record on mixed *G. ruber* and *G. elongatus* (previously referred to as *G. ruber* s.s. and s.l., respectively) from the nearby core site MD05-2920 [Tachikawa et al., 2014] (see supplementary information for details). The MD05-2920 Mg/Ca record has been converted to temperature by using the multispecies Mg/Ca-temperature calibration of Anand et al., [2003]. Our interpretation, however, does not depend on the choice of calibrations (see supplementary information for details). To estimate the oxygen isotope composition of seawater ($\delta^{18}O_{SW}$) from Mg/Ca-based temperatures and shell $\delta^{18}O$ of *G. ruber* and *P. obliquiloculata*, we applied the high-light $\delta^{18}O$-temperature equation of Bemis et al., [1998]:

$$T(^{\circ}C) = 14.9 - 4.8\,(\delta^{18}O - \delta^{18}O_{SW})$$

The resulting values were converted to Vienna Standard Mean Ocean Water (VSMOW) by adding 0.27‰ [Hut, 1987] and corrected for changes in global ice volume following Waelbroeck et al., [2002].

In order to track changes in the stratification of the upper water column, we calculated the difference between *G. ruber* and *P. obliquiloculata*-based temperatures (ΔT). Since Mg/Ca and $\delta^{18}O$ of *G. ruber* are from different cores (MD05-2920 and GeoB 17419-1), we aligned the age scales of the relevant records prior to the calculation of $\delta^{18}O_{SW}$ and ΔT by resampling the relevant records at intervals of 500 years.

The estimation of temperature and $\delta^{18}O_{SW}$ uncertainties followed the conservative approach described in Mohtadi et al., [2014] and is based on propagation of uncertainties introduced by Mg/Ca and $\delta^{18}O$ measurements, the Mg/Ca-temperature calibrations and/or the $\delta^{18}O$-temperature equation as well as the global ice volume estimate (±0.09‰) [Waelbroeck et al., 2002]. We also estimated the uncertainties of the already published surface temperatures to calculate uncertainties in ΔT. Here, the mean external reproducibility as reported by Tachikawa et al., [2014] was assumed as uncertainty estimate for Mg/Ca. Estimates of ΔT uncertainties are based on propagation of temperature uncertainties. Resulting temperature uncertainties average about 1 °C for SST, 2 °C for thermocline temperatures and about 3 °C for ΔT. For $\delta^{18}O_{SW}$ uncertainties average 0.3‰ for the surface and 0.5‰ for the thermocline.

4. Results

4.1. Age model and benthic $\delta^{18}O$

Benthic $\delta^{18}O$ (*C. wuellerstorfi*) reveals that core GeoB 17419-1 covers the last 110 kyr (Fig. 3) with an average temporal resolution of about 0.5 kyr/sample. The record is characterized by glacial–interglacial variations representing Marine Isotope Stages (MIS) with higher $\delta^{18}O$ values during MIS 2 and 4 and lower values during MIS 1, 3 and 5 (Fig. 3). The substages MIS 5a, b and c are clearly recognizable (Fig. 3).

4.2. Planktic $\delta^{18}O$ and Mg/Ca temperatures

Shell $\delta^{18}O$ of *G. ruber* varies between −2.75 and −0.92‰ (Fig. 3a), $\delta^{18}O$ of *P. obliquiloculata* varies between −1.84 and 0.47‰ (Fig. 3b). Both records follow the MIS and show $\delta^{18}O$ maxima during MIS 2 and minima during the Holocene.

The shell Mg/Ca record of *P. obliquiloculata* varies between 1.63 and 3.57 mmol/mol, which converts into temperatures of ~21.1 and 28.4 °C (Fig. 4b). Minimum temperatures (21.1 °C) occur during MIS 4, maximum temperatures (28.4 °C) during the early Holocene. With ~25.1 °C, modern temperatures are only slightly warmer than during the LGM (~24.2 °C) and temperatures during MIS 3–4 and MIS 5a–d are comparable. The record indicates slightly increasing temperatures during MIS 5c and declining temperatures during MIS 5a, interrupted by a single data point that marks cooler temperatures during MIS 5b. The interval between 69.8 and 65.2 ka (within MIS 4) is marked by cool temperatures averaging 22.2 °C. The record depicts an abrupt temperature increase of about 2–3 °C late in MIS 4 that is followed by a declining trend until approximately 30 ka, and then a rise to maximum temperature of ~28.4 °C during the early Holocene (~10.5 ka). The warming trend is interrupted by a temperature plateau during the LGM. The Holocene is characterized by a cooling trend of about 2.0–2.5 °C.

The ΔT record (*G. ruber* - *P. obliquiloculata*) shows a stepwise decreasing trend towards the LGM and an increase afterwards (Fig. 4c). Maximal values up to ~5.0 °C are measured between 110 and 65–66 ka. Coeval with the abrupt warming indicated by *P. obliquiloculata* at 65/66 ka, the ΔT estimates reveal a decrease with an amplitude of 3.2 °C. ΔT remains relatively constant during MIS 3, reaches minimum values averaging ~1.3 °C during MIS 2, and then increases towards the present.

The *G. ruber* $\delta^{18}O_{SW}$ record is characterized by high frequency oscillations with values ranging between −0.09 and 1.00‰ (Fig. 4d). *G. ruber* indicates exceptionally low $\delta^{18}O_{SW}$ from 74 to 66 ka and from about 28 to 18 ka. The $\delta^{18}O_{SW}$ of *P. obliquiloculata* ranges between 0.14 and 2.05‰ (Fig. 4e). The record depicts glacial–interglacial variations with lower (higher) values during interglacial (glacial) periods, superimposed by higher frequency oscillations.

4.3. Nd/Ca in P. obliquiloculata and bulk sediment Ti/Ca

The *P. obliquiloculata*-based Nd/Ca record ranges between 0.0 and 1.4 μmol/mol (Fig. 5c). Relatively high values are recorded between 77 and 58 ka and between 27 and 14 ka.

Bulk sediment Ti/Ca ratios, presented as ln (Ti/Ca) shows high frequency oscillation with values ranging between −3.8 and −2.5. Higher ratios are recorded around 102 ka, 72–64 ka, from about 26 to 16 ka and after 2 ka (Fig. 5b).

5. Discussion

5.1. Obliquity-controlled variations of WPWP thermocline temperature

Variations in the Mg/Ca-derived temperature record of *P. obliquiloculata* are interpreted to reflect variations in thermocline temperature. In principle, changes in the calcification depth of the foraminifera could additionally influence the temperature record. However, the calcification depth of *P. obliquiloculata* depends on environmental conditions. Studies on the modern ocean show that the calcification depth of *P. obliquiloculata* mainly corresponds to the depth of the deep chlorophyll maximum (DCM) [e.g. Fairbanks et al., 1980] and that the DCM in the WPWP varies with the thermocline depth [Radenac and Rodier, 1996; Radenac et al., 2016]. Besides, we neither observe exceptionally large amplitudes within the stable carbon isotope ($\delta^{13}C$) records nor covariations between $\delta^{13}C$ and Mg/Ca-based temperatures (Fig. S3), which would be expected if thermocline temperature variations were dominated by

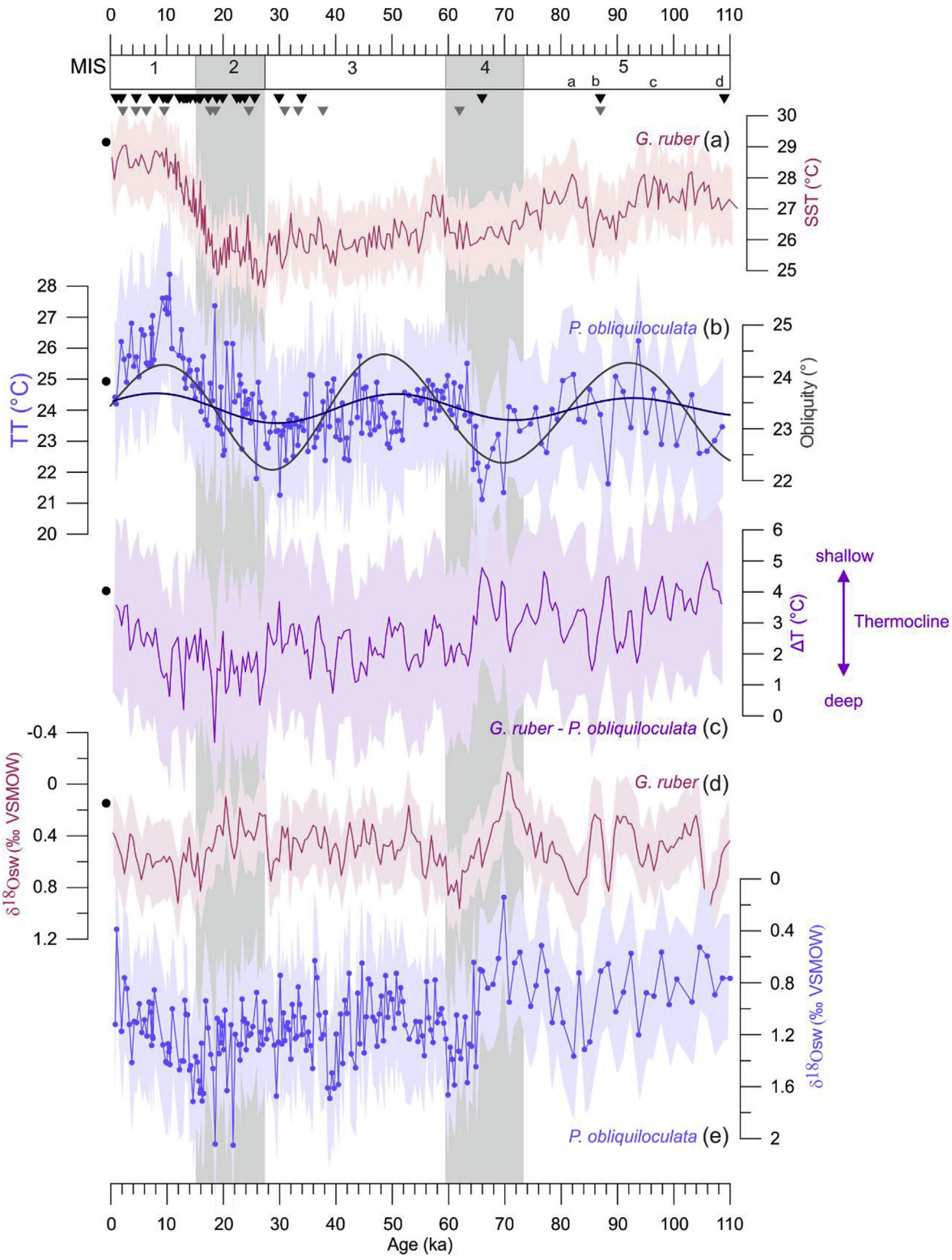

Fig. 4. Mg/Ca derived temperature and $\delta^{18}O_{SW}$ records of core GeoB17419-1. For comparison we also show the sea surface temperature record of MD05-2920 [Tachikawa et al., 2014] that was used to estimate the surface $\delta^{18}O_{SW}$ and ΔT. (a) Sea surface temperature estimates of MD05-2920 on a revised age scale (see supplementary information S1). (b) Thermocline temperature estimates from GeoB 17419-1. The dark blue line shows the bandpass-filtered thermocline temperature signal (see section 5.1). The gray solid line indicates variations in the Earth's obliquity [Laskar, 1990]. (c) Surface–thermocline temperature gradient (ΔT; *G. ruber - P. obliquiloculata*). (d) Surface $\delta^{18}O_{SW}$ calculated from *G. ruber*-based temperatures of MD05-2920 and $\delta^{18}O$ of GeoB17419-1. (e) *P. obliquiloculata*-based thermocline $\delta^{18}O_{SW}$ of GeoB17419-1. Triangles depict dating points of GeoB 17419-1 (black) and MD05-2920 (gray). Shadings represent 1σ-uncertainties (see section 3.4). Black dots reflect modern conditions as indicated by core top data from the multi core GeoB 17419-2 [Hollstein et al., 2017]. Marine Isotope stages (MIS) 1–5 as dated by Sanchez Goñi and Harrison [2010] are indicated at the top. Gray bars indicate MIS 2 and 4. The $\delta^{18}O_{SW}$ records are corrected for changes in ice volume. (For interpretation of the references to color in this figure legend, the reader is referred to the Web version of this article.)

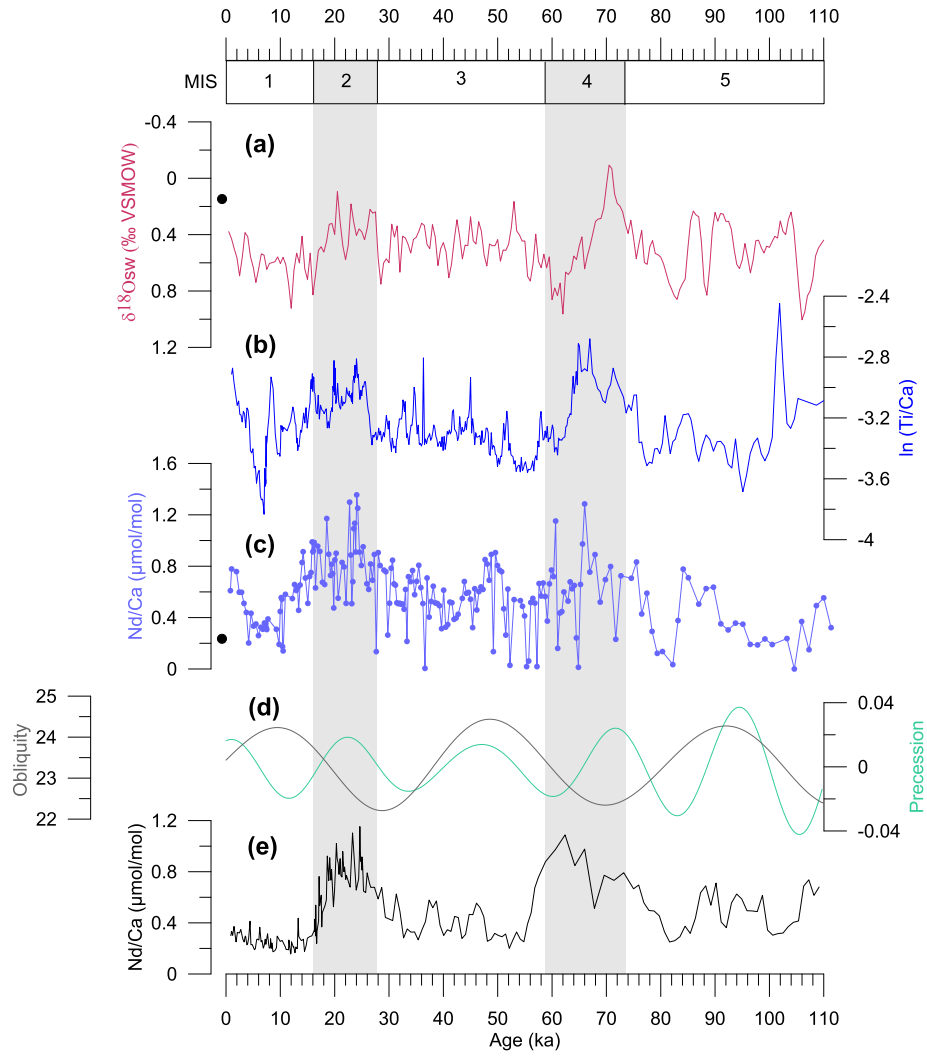

Fig. 5. PNG precipitation records. (a) *G. ruber* $\delta^{18}O_{SW}$, (b) ln(Ti/Ca), (c) *P. obliquiloculata* Nd/Ca of GeoB 17419-1 in comparison to (e) *G. ruber* Nd/Ca of MD05-2925 (see Fig. 1 for site location) [Liu et al., 2015]. (d) Variations in the Earth's obliquity (gray) and climatic precession (green) [Laskar, 1990]. Black dots reflect modern conditions as indicated by core top data from the multi core GeoB 17419-2 [Hollstein et al., 2017]. Marine Isotope stages (MIS) 1–5 as dated by Sanchez Goñi and Harrison [2010] are indicated at the top. Gray bars mark glacial periods MIS 2 and 4. (For interpretation of the references to color in this figure legend, the reader is referred to the Web version of this article.)

vertical migration of *P. obliquiloculata*, as surface waters are marked by higher $\delta^{13}C$ values than the SPTW.

The Mg/Ca-derived thermocline temperature record of GeoB17419-1 depicts quasi-cyclic variations, which appear to co-vary with variations in Earth's obliquity. Visual inspection indicates that *P. obliquiloculata* records higher (lower) temperatures during periods of increased (decreased) obliquity (Fig. 4b). For example, the exceptionally early onset of deglacial warming (starting around 30 ka) reflected by the *P. obliquiloculata* temperature estimates is unlikely to be due to changes in the glacial–interglacial boundary conditions but mostly coincides with an increase in obliquity. In addition, the record indicates a 2.0–2.5 °C cooling of thermocline temperatures throughout the Holocene, which is coeval with a decrease in obliquity. Such a Holocene cooling trend is also observed in other thermocline temperature records from the western Pacific and Indonesian Seas [e.g. Bolliet et al., 2011; Dang et al., 2012; Rosenthal et al., 2013].

We filtered the temperature record with a Gaussian band-pass filter centered at a frequency of 0.02439 ± 0.007 (corresponding to periods of 31.5–58.6 kyr) (Fig. 4b) to emphasize cyclic variations in the obliquity band of 41 kyr. Filtering was done with Astrochron (R package for astrochronology) [Meyers, 2014]. The specific shape of the resulting curve (amplitude and exact phase) varies with the chosen filter parameters. However, independent of the parameters the filtered signal co-varies with obliquity. Additionally, we performed a spectral analysis to assess the statistical significance of cyclic variations on the obliquity band. In order to exclude long-term (glacial–interglacial) variations from the spectral analysis we eliminated frequencies below 0.018 kyr^{-1} from the temperature record. The spectral analysis was performed with REDFIT [Schulz and Mudelsee, 2002]. The results confirm that the thermocline temperature record is characterized by cyclic variations that correspond to the periodicity of obliquity (Fig. 6a). The power spectrum depicts a statistically significant peak at a frequency of 0.024 kyr^{-1}, which corresponds to a period of 41 kyr. We thus infer that obliquity has a significant impact on WPWP thermocline temperatures. This is also in accordance with modeling studies, which demonstrate that an increase (decrease) in obliquity leads to a warming (cooling) of tropical Pacific subsurface temperatures [Lee and Poulsen, 2005; Mantsis et al., 2011].

Variations in the Earth's obliquity only have a very small influence on low-latitude insolation, and SSTs recorded in MD05-2920

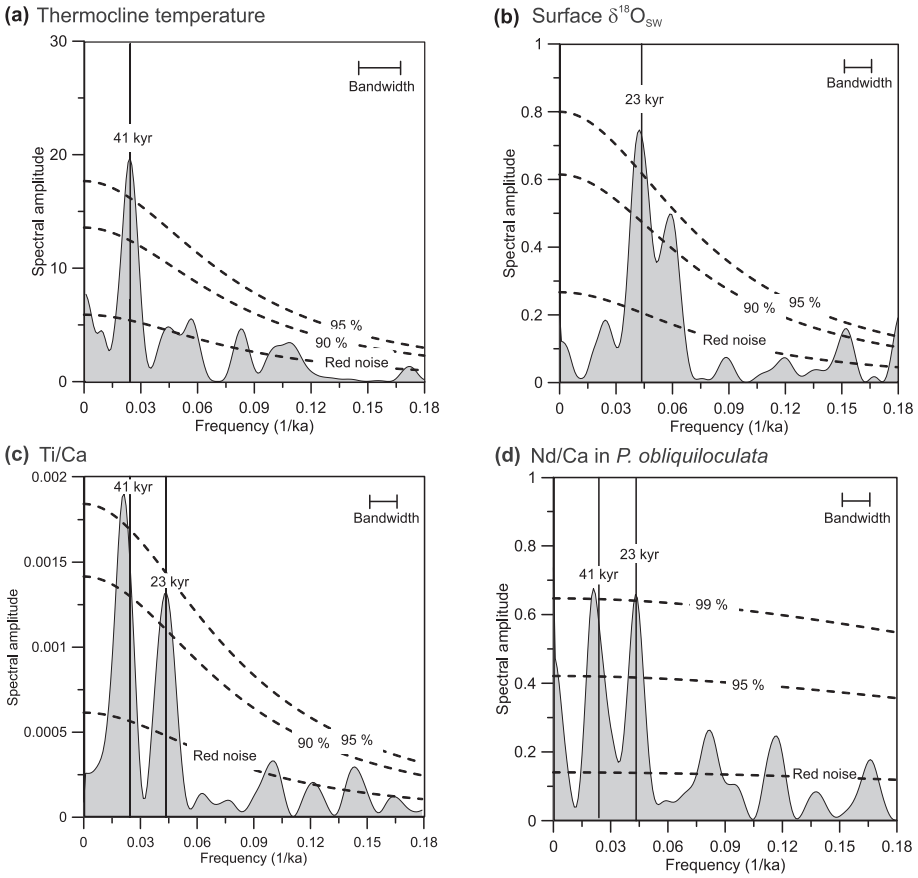

Fig. 6. Spectral analyses of thermocline and surface records. (a) Thermocline temperature (GeoB 17419-1), (b) surface $\delta^{18}O_{SW}$ (combined GeoB17419-1 and MD05-2920), (c) Ti/Ca and (d) *P. obliquiloculata* Nd/Ca (GeoB 17419-1). The analyses were performed with REDFIT [Schulz and Mudelsee, 2002]. An oversampling factor of 9 was chosen to increase the resolution of samples frequencies. The bandwidth is 6 dB. We used a Welch type spectral window. Dashed lines indicate the red-noise spectrum as well as 90 and 95% confidence levels. Solid vertical lines denote frequencies that correspond to obliquity (41 kyr) or precession (23 and 19 kyr) periodicities.

do not show a dominating influence of obliquity [see also Tachikawa et al., 2014]. Thus, we suggest that obliquity-related thermocline temperature fluctuations are caused by remote forcing on southern mid-latitude climate variations. Most likely warming (cooling) of thermocline waters at the core site during periods of increased (decreased) obliquity is caused by a reduced (intensified) ventilation and advection of the SPTW [Lee and Poulsen, 2005]. Similar mechanisms have been proposed earlier to explain the temperature drops observed in many Holocene records from the WPWP and the Indonesian Seas [e.g. Rosenthal et al., 2013; Rosenthal et al., 2017]. Indeed, numerical simulations indicate a weakening of subtropical trades and mid-latitude westerlies that is associated with a reduction in meridional (equator-pole) insolation and surface pressure gradients during periods of increased obliquity and which causes a weakening of the subtropical gyre circulation [Lee and Poulsen, 2005; Mantsis et al., 2011; Timmermann et al., 2014]. A weakening in the subtropical gyre circulation could diminish both the subduction and advection of relatively cool waters from the subtropical Pacific and the heat export from the tropical Pacific, and thus lead to a warming of subsurface temperatures in the WPWP [Lee and Poulsen, 2005; Mantsis et al., 2011; Qu et al., 2013].

In accordance with numerical modeling simulations the SST record of MD05-2920 and ΔT record between MD05-2920 and GeoB 17419-1 do not show dominant variations at the obliquity periodicity, indicating that the warming observed in the WPWP thermocline during periods of high obliquity does not penetrate to the sea surface and has only minor effects on the WPWP thermocline depth [Lee and Poulsen, 2005; Mantsis et al., 2011].

Previous studies provide conflicting results regarding the significance of the response of the equatorial ocean and atmospheric circulation systems to obliquity and the related processes outlined above. For instance, the early model of *Lee and Poulsen* [2005] suggests that obliquity has only little effects on the equatorial atmospheric circulation. In contrast, recent modeling studies suggest that obliquity exerts a direct influence on tropical Pacific precipitation via complex reorganizations of the Hadley circulation that are related to obliquity-controlled changes in the inter- and intra-hemispheric insolation gradients [Bosmans et al., 2015; Mantsis et al., 2011; Mantsis et al., 2014; Rachmayani et al., 2016]. For instance, these studies propose a weakening of the annual mean Hadley circulation and a reduced ITCZ rainfall intensity when obliquity is high [Bosmans et al., 2015; Mantsis et al., 2011]. We address a potential influence of obliquity on rainfall above PNG and the ambient ocean, in section 5.2. In section 5.3 we then focus on variations in thermocline depth and related changes in the Walker circulation and the underlying forcing.

5.2. Orbital-controlled variations in regional precipitation

Proxy-based and numerical modeling studies consistently indicate a strong control of precession on precipitation over PNG and the ambient ocean with enhanced precipitation when precession is high [Dang et al., 2015; Kutzbach et al., 2008; Liu et al., 2015;

Tachikawa et al., 2011]. An increase in precipitation under high precession is attributed to a southward shift in the position of the ITCZ, an intensification of its rainfall intensity [Merlis et al., 2013], and an increase of the Australian monsoon. Additionally, an obliquity control on PNG precipitation is suggested by climate model simulations that indicate suppressed precipitation over PNG during periods of high obliquity [e.g. Bosmans et al., 2015; Liu et al., 2015; Mohtadi et al., 2016; Rachmayani et al., 2016]. Results of proxy records on the influence of obliquity are ambiguous: Records of bulk sediment elements and its ratios from the Halmahera Sea north of PNG does not show an obliquity influence [Dang et al., 2015]. Tachikawa et al., [2011] used bulk sediment elements and its ratios, such as Ti/K and Ti/Ca, in core MD05-2920 to assess past variations in continental runoff and hence precipitation above PNG with high (low) Ti/K or Ti/Ca being indicative for increased (decreased) precipitation. The MD05-2920 records consistently indicate that rainfall above PNG varies in response to precession with enhanced (decreased) precipitation when precession is high (low) [Tachikawa et al., 2011]. The Ti/Ca record additionally shows a statistically significant obliquity influence with low Ti/Ca corresponding to high obliquity and vice versa. Our Ti/Ca record of GeoB 17419-1 is in close correlation to the Ti/Ca record of MD05-2920 and thus shows comparable variations (Figs. 5b and 6c and S1). However, as discussed in detail in Tachikawa et al., [2011] the obliquity-related variations in Ti/Ca may be related to variations in carbonate content.

An obliquity control on PNG precipitation was suggested on the basis of Nd/Ca measured on *G. ruber* from core MD05-2925, retrieved at the southern tip of PNG (see Figs. 1 and 5) [Liu et al., 2015]. Here, we use Nd/Ca in *P. obliquiloculata* samples of GeoB 17419-1 as indicator for continental rainfall over PNG. We assume that seawater Nd is principally delivered by fine particles originating from PNG because elevated Nd concentrations are reported within the Bismarck Sea downstream the Sepik River [Grenier et al., 2013]. Provenance studies consistently indicate that increased particulate concentrations of REEs in the western equatorial Pacific are river-derived [Sholkovitz et al., 1999; Tachikawa et al., 2011]. We therefore interpret enhanced *P. obliquiloculata* Nd/Ca concentrations to be associated with increased precipitation and the discharge of the Sepik River. An additional dust input of Nd from volcanic sources is possible [Grenier et al., 2013]. Seawater Nd particles can either be incorporated into the foraminifera tests within the water column [Liu et al., 2015; Martínez-Botí et al., 2009] or added as secondary calcite overgrowth on the foraminifera tests after deposition [Roberts et al., 2012, Rosenthal, unpublished data; Tachikawa et al., 2013]. Our record indicates that Nd/Ca varies in response to precession with high (low) Nd/Ca when precession is high (low) (Figs. 5c and 6d). Additionally, the power spectrum of the record shows a significant peak in the obliquity band indicating an additional influence of obliquity with low Nd/Ca corresponding to high obliquity and vice versa (Figs. 5c and 6d). However, like the Ti/Ca signal, the Nd/Ca obliquity signal could be related to variations in carbonate contribution. Additionally, the obliquity-driven variations in both, the Ti/Ca and Nd/Ca records could be caused by changes in advection and the strength of the equatorial western boundary currents, namely NGCC and NGCUC, while we exclude the influence of advection on the proxy records on the timescale of variations in precession (see explanation further below). As indicated in section 5.1, a weaker subtropical gyre circulation during periods of high obliquity could cause a weakening of the NGCC and NGCUC and subsequently reduce the transport of Ti and Nd particles to the core site.

To further assess precipitation changes in the marine environment, we use the $\delta^{18}O_{SW}$ record of *G. ruber*. The *G. ruber* $\delta^{18}O_{SW}$ reveals cyclic variations with low (high) $\delta^{18}O_{SW}$ corresponding to precession maxima (minima) (Figs. 5a and 6b). We interpret variations in $\delta^{18}O_{SW}$ to be primarily controlled by variations in the amount of precipitation over the core location. A time series of $\delta^{18}O_{SW}$ data from Manus Island (PNG, Fig. 1) shows that variations in the oxygen isotopic composition of seawater closely correlate with variations in salinity, evaporation and precipitation with lower $\delta^{18}O_{SW}$ corresponding to less saline conditions, but enhanced evaporation and precipitation, and vice versa [Conroy et al., 2017] indicating that $\delta^{18}O_{SW}$ in the study area is primarily controlled by local precipitation. Continental precipitation over PNG and river runoff could additionally influence the $\delta^{18}O_{SW}$ record, since the sites GeoB 17419-1 and MD05-2920 are located relatively close (100–150 km) to the Sepik river mouth (Fig. 1) [see also Tachikawa et al., 2011].

Changes in the isotopic composition of rainfall caused by shifts in the source area, and variations in oceanic advection or upwelling could in principle additionally affect the surface $\delta^{18}O_{SW}$ at the study site. However, as we assume that the water vapor over the past glacial-interglacial cycle, has been constantly sourced from the nearby ocean, associated variations in the $\delta^{18}O_{SW}$ are expected to be negligible. By analogy to seasonal changes observed in the modern ocean, the NGCC would be expected to strengthen when precession is low, and the core sites would be more strongly affected by freshwater from PNG. Precession-related alterations in oceanic advection would thus counteract the precession signal observed in the $\delta^{18}O_{SW}$ record. Likewise, the effect of wind-driven upwelling would counteract the observed signal. If upwelling affected the core site, it is expected to be stronger when precession is high.

In contrast to the Ti/Ca and Nd/Ca records, the surface $\delta^{18}O_{SW}$ does not show a statistically significant obliquity influence. This divergence between the Ti/Ca, Nd/Ca and the $\delta^{18}O_{SW}$ records indicates either a decoupling between continental and oceanic rainfall or secondary effects on the Ti/Ca and Nd/Ca records in the obliquity band.

Taken together, our Ti/Ca, foraminiferal Nd/Ca and $\delta^{18}O_{SW}$ records clearly support previous proxy-based and numerical modeling studies that indicate a strong control of precession on the tropical monsoon system, the position of the ITCZ, and ultimately on precipitation over PNG and the ambient ocean with enhanced precipitation when precession is high [Dang et al., 2015; Kutzbach et al., 2008; Liu et al., 2015; Tachikawa et al., 2011]. Records from the northern WPWP also indicate an increase in precipitation under high precession [Fraser et al., 2014; Kissel et al., 2010]. The coherence of the marine records from the northern and southern WPWP implies a uniform response of rainfall across the tropical western Pacific Ocean to precession. A southward shift of the ITCZ would be accompanied by an increase in mean annual rainfall over the northern and southern WPWP during high obliquity. In addition, our Ti/Ca and Nd/Ca agree with previous records from PNG [Liu et al., 2015; Tachikawa et al., 2011] that, in contrast to records from the Halmahera Sea [Dang et al., 2015], show an obliquity signal. However, on the basis of our data, we cannot resolve whether the variability in the obliquity band is related to continental rainfall or other effects.

5.3. LGM thermocline depth anomaly and implications for the Pacific Walker circulation

Variations in the ΔT (*G. ruber* − *P. obliquiloculata*) are interpreted as changes in the thermocline depth with a large (small) ΔT corresponding to a shallow (deep) thermocline [Bolliet et al., 2011; Steinke et al., 2010; Xu et al., 2008]. Our ΔT record reflects a stepwise thermocline deepening at the core location towards the LGM and a shoaling afterwards (Fig. 4c). During the interglacial substages MIS 5a–d the thermocline was relatively shallow. The strong

decrease in ΔT starting around 66–65 ka indicates a deepening of the thermocline during MIS 4. The LGM is characterized by a minimum in ΔT indicating the weakest thermal stratification during the past 110 kyr. From the LGM until the present an increasing ΔT denotes a gradual thermocline shoaling. As inferred from $\delta^{18}O_{SW}$ of *P. obliquiloculata*, the LGM thermocline deepening coincides with more saline conditions within the upper thermocline (Fig. 4b and e).

The apparent glacial–interglacial ΔT variability is superimposed by other variations. The beginning of MIS 4 for instance is characterized by a very shallow thermocline, and the thermocline during the early Holocene is as deep as during MIS 3. This is reasonable because variations in ΔT are associated with both variations in surface and thermocline temperatures, and are thus, presumably, also controlled by obliquity, which has a strong influence on the thermocline temperature record (see section 5.2.), and by precession, which has a clear influence on the surface temperature record [Tachikawa et al., 2014]. However, neither obliquity- nor precession-controlled fluctuations are significant in the ΔT record (Fig. S4).

As the LGM is characterized by the largest ΔT anomaly and hence, the deepest thermocline over the past 110 kyr, we will focus on the LGM thermocline depth anomaly and underlying forcing mechanism in the following. Published reconstructions from the western equatorial Pacific and Indian Ocean based on a wide range of proxies are inconsistent, with some studies suggesting thermocline deepening [e.g. Andreasen and Ravelo, 1997; Patrick and Thunell, 1997] and others suggesting shoaling [e.g. Leech et al., 2013; Regoli et al., 2015; Sagawa et al., 2012] during the LGM. To analyze the spatial pattern of thermocline depth anomalies during the LGM relative to the present we compile ΔT records from the WPWP (Table S1 and Figs. 7 and 8a). We use exclusively Mg/Ca-based ΔT records as this proxy has been shown to be a robust indicator of relative thermocline depth (TCD) in previous studies [e.g. Mohtadi et al., 2017]. This way we also avoid potential discrepancies associated with the use of different proxies. Furthermore, we do not include the ΔT records published by de Garidel-Thoron et al., [2007] and Regoli et al., [2015], because these records are based on foraminifera species that presumably calcify within the mixed layer [Hollstein et al., 2017]. To assure the comparability of the ΔT records used, we apply the same calibrations to all records, but corrected for different cleaning methods (reductive vs. non-reductive) by assuming a 10% Mg/Ca loss due to reductive cleaning [e.g. Barker et al., 2003; Martin and Lea, 2002; Rosenthal et al., 2004]. However, the choice of calibrations does not affect the overall spatial pattern of TCD anomalies. The compilation of the hitherto available ΔT records illustrates a dipole-like pattern with a LGM thermocline shoaling in the northern WPWP (core 3cBx) [Sagawa et al., 2012], no change within the central WPWP (MD06-3067 and ODP806) [Bolliet et al., 2011; Ford et al., 2015] and a deepening in the southern WPWP (GeoB 17419-1/MD05-2920; this study) (Figs. 7 and 8a).

The northern record of 3cBx exhibits a LGM (19 – 23 ka) to late Holocene (core top) ΔT change of 2.1 °C. The decrease in ΔT at this site is confirmed by other surface-thermocline ΔT records (*G. ruber* – *G. conglobatus* and *G. ruber* – *G. menardii*) of the same core [Sagawa et al., 2012]. Our southern WPWP record shows a ΔT increase of 2.6 °C from the LGM to the present (modern core top of GeoB 17419-2). However, the ΔT record from the central WPWP (ODP site 806) [Ford et al., 2015] consists of only two time slices (LGM and late Holocene), which are characterized by similar ΔT values (5.8 and 5.9 °C, respectively). Likewise, the ΔT record of MD06-3067 (offshore Mindanao) [Bolliet et al., 2011] does not cover the late Holocene. For this site, the evolution of the thermocline depth from the LGM to the present cannot be assessed

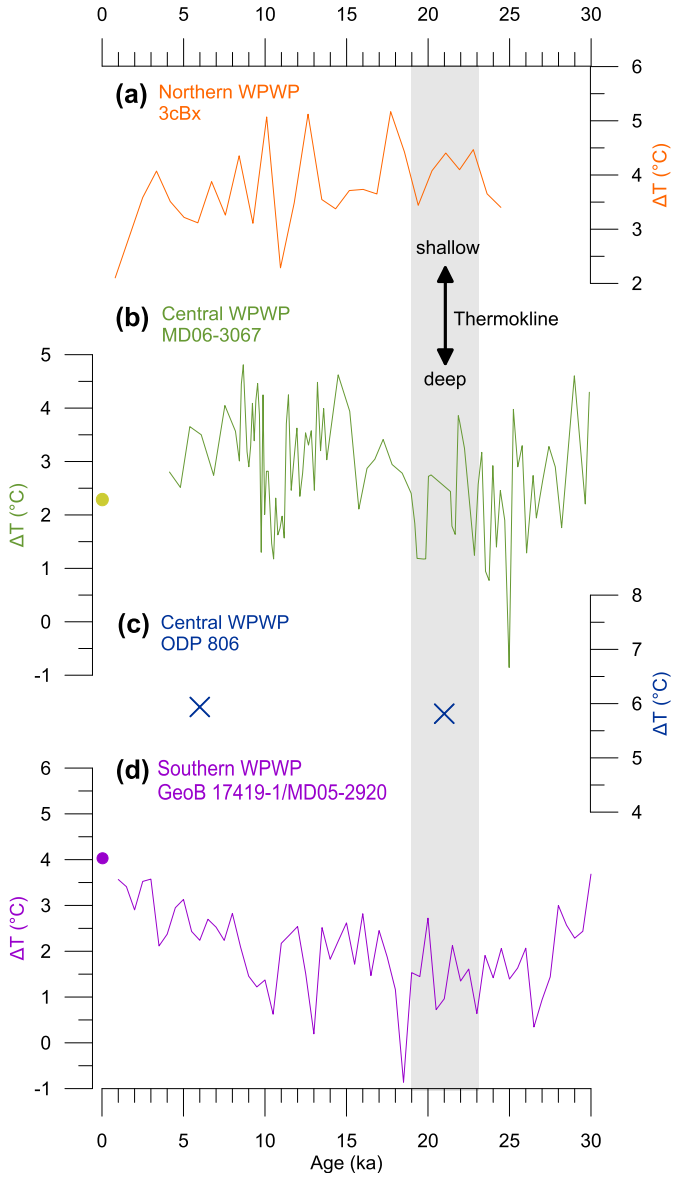

Fig. 7. Mg/Ca-based ΔT reconstructions for the WPWP. (a) *G. ruber* – *P. obliquiloculata* ΔT of 3cBx [Sagawa et al., 2012], (b) *G. ruber* – *P. obliquiloculata* ΔT of MD06-3067 [Bolliet et al., 2011]. The light green dot indicates the *G. ruber* – *P. obliquiloculata* ΔT of modern surface sediments from the nearby located site RR1313-24 50MC [Hollstein et al., 2017]. (c) Late Holocene and LGM *G. sacculifer* – *G. tumida* ΔT of ODP 806 [Ford et al., 2015], (d) *G. ruber* – *P. obliquiloculata* ΔT of GeoB 17419-1/MD05-2920 (this study). The ΔT estimate of site ODP806 is based on an average of Mg/Ca-temperature on individual foraminifera samples. The samples are not accurately dated, but correspond to the late Holocene and the LGM. The LGM is marked by a gray bar. (For interpretation of the references to color in this figure legend, the reader is referred to the Web version of this article.)

with certainty. Over the last 160 kyr, the ΔT record of core MD06-3067 generally indicates a trend towards a deeper (shallower) thermocline during glacial (interglacial) periods [Bolliet et al., 2011]. However, data from modern surface sediments from a nearby site (RR1313-24 50MC; 13.57°N, 123.73°E; off Philippines) [Hollstein et al., 2017] indicates a modern temperature gradient of 2.3 °C, essentially the same as the ΔT of 2.2 °C recorded by MD06-3067 during the LGM (Fig. 7c), thus providing evidence that the thermocline depth in the central WPWP remained relatively constant between the LGM and the present.

In order to better understand the mechanisms that led to the

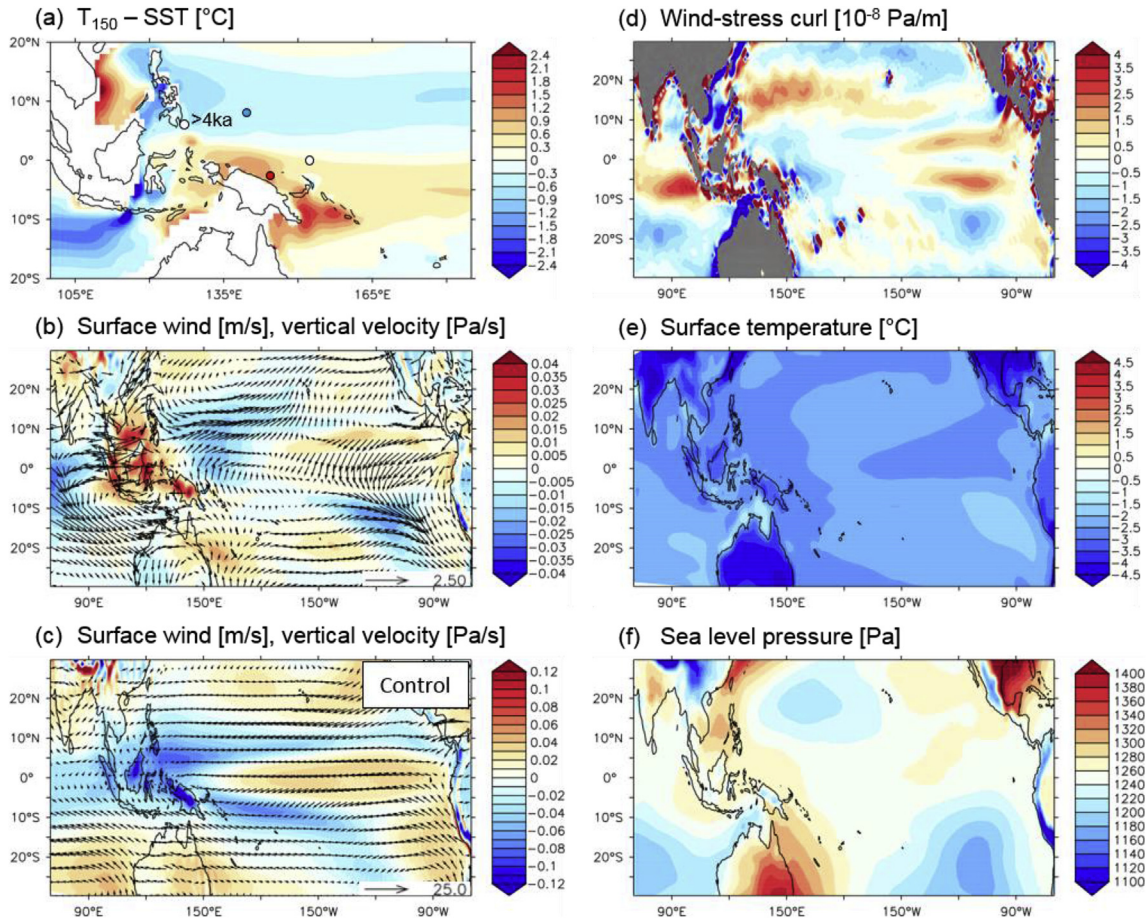

Fig. 8. Tropical Pacific (annual mean) thermocline and climate conditions as simulated by the MRI-CGCM3 coupled general circulation model (PMIP3/CMIP5 simulations). All panels show LGM anomalies relative to the pre-industrial control run, except for panel (c) which shows pre-industrial control run fields. (a) Ocean subsurface (150 m) minus surface temperature difference in the WPWP as a measure for thermocline depth (red and blue colors indicate thermocline deepening and shoaling, respectively); colored dots represent proxy records discussed in this study [Bolliet et al., 2011; Ford et al., 2015; Sagawa et al., 2012], from which LGM thermocline depth changes have been inferred (red and blue indicate thermocline deepening and shoaling, white indicates a comparable thermocline depth). (b) Surface (925 hPa) winds and mid-troposphere (500 hPa) vertical velocity (red and blue colors indicate descent/ascent). Note that the field of wind-stress anomaly shows major structures almost identical to the field of surface wind anomaly and is therefore not shown here. (c) Same as (b) but for control to help interpret the LGM circulation anomaly pattern. (d) Wind-stress curl over the ocean. (e) Surface land and ocean temperature. (f) Sea level pressure (Pa). Note the different map section in (a) and (b–f). Modern coastlines are shown in all plots. (For interpretation of the references to color in this figure legend, the reader is referred to the Web version of this article.)

spatial pattern of TCD anomalies depicted in Fig. 8a, we compared the reconstructed LGM thermocline depth anomaly pattern with the output of 14 available PMIP2 and PMIP3/CMIP5 climate model simulations of the LGM [Braconnot et al., 2007; Harrison et al., 2015]. All models consider LGM boundary conditions, such as reduced greenhouse gas concentrations, altered astronomical parameters and ice sheet extent. The specifications of the individual models are provided in the supplement (Table S2). We identify MRI-CGCM3 as the only model that captures the asymmetric TCD anomaly pattern that we inferred from the ΔT records (Table S2, Fig. S5). In this model, changes in vertical temperature gradients are qualitatively in accordance with reconstructed values at the core sites (Fig. 8a). It is unclear why MRI-CGCM is the only model that captures the TCD anomaly pattern indicated by the proxy data. Differing resolution, atmospheric convection and land-surface schemes may play a role. In MRI-CGCM3, the TCD anomaly pattern is to a large extent attributable to LGM wind-field anomalies (Fig. 8b and c) and associated Sverdrup dynamics [DiNezio et al., 2011; Leech et al., 2013], through which the western Pacific TCD becomes a function of wind stress and curl, integrated from the eastern side of the basin towards the west, in the direction of Rossby waves [Tomczak and Godfrey, 2003]. A large region of positive wind-stress curl in the southeastern equatorial Pacific (Fig. 8d) creates Ekman convergence, which sets the stage for an overall deepening of the thermocline in the glacial tropical Pacific south of the equator. Regions of glacial wind-stress anomalies with an easterly component in the tropical West Pacific (Fig. 8b) further tend to deepen the thermocline there. In addition, particularly large glacial thermocline deepening off the coast of New Guinea, which also affects the TCD at site GeoB 17419-1, is favored by strong alongshore southeasterly wind anomalies (Fig. 8b). Glacial thermocline shoaling in the northern tropical West Pacific as recorded in proxy records of core 3cBx [Sagawa et al., 2012] is associated with strong westerly wind-stress anomalies and a positive anomalous wind-stress curl north of about 10°N (Fig. 8b,d).

In MRI-CGCM3, the LGM annual-mean wind system over the tropical West Pacific, which shapes the TCD anomaly pattern, is characterized by reduced convection over the Maritime Continent, whereas enhanced ascent takes place over the western Pacific (Fig. 8b). The associated change in the equatorial wind circulation can be interpreted as a contraction of the Pacific Walker cell on its western side (Figs. 8b and S6) compared to the modern situation (Fig. 8c). In contrast to the prediction of simple hydrologic-thermodynamic considerations [Soden and Held, 2006; Vecchi

et al., 2006], the strength of the Pacific Walker circulation does not increase in the colder climate of the LGM. Instead, reduced convection over the Maritime Continent is attributable to the relatively strong (compared to the surrounding sea surface) land surface cooling (Fig. 8e), which is primarily related to the different evaporation response of land and ocean to the glacial cooling as well as to land–surface feedbacks [Braconnot et al., 2012].

Around Indonesia, a "Gill-type" circulation response results from the reduced convection, with anomalous surface wind divergence over the Maritime continent (Fig. 8b) and two areas of anomalous high sea-level pressure (SLP) centered north and south of the equator (Fig. 8f) [Gill, 1980]. The locations of these highs are modified by the continental configuration, with one anticyclone over the South China Sea and the other one shifted over Australia and substantially strengthened probably due to substantial surface cooling there (Fig. 8e and f). As a result of this hemispherically asymmetric SLP distribution, anomalous cross-equatorial southerly wind occurs east of the Maritime Continent (Fig. 8b). Over the South China Sea, the wind-stress curl associated with the high pressure anomaly causes the thermocline to deepen, consistent with regional TCD reconstructions (Fig. 8a,d) [Xu et al., 2010 and references therein].

We note that MRI-CGCM3 suggests a decrease in precipitation over PNG during the LGM in comparison to the preindustrial period (inferred from vertical velocity; Fig. 8b), while the precipitation records (Ti/Ca and *P. obliquiloculata* Nd/Ca) indicate similar to enhanced precipitation over PNG during the same period (see section 5.3). This discrepancy may be related to the fact that the model does not resolve the regional topographic features of PNG. Overall, our proxy records indicate that the regional precipitation variability is governed by astronomically-driven changes in the monsoon system and the ITCZ rather than by changes in the Walker circulation that relate to varying glacial-interglacial boundary conditions. This is also in accordance with observations of the modern ocean, which indicate that variations in the state of the Pacific Ocean and the Walker circulation do not have a clear impact on the rainfall within the study area (see section 2).

In summary, our model-data comparison suggests a substantial change in the Pacific Walker circulation during the LGM compared to the modern one with enhanced ascent over the western equatorial Pacific, and drastically reduced convection over the Maritime Continent. A recent study by Mohtadi et al., [2017] suggests a stronger-than-modern glacial Indian Ocean Walker circulation with enhanced ascent over the eastern equatorial Indian Ocean. Taken together, and in view of the weakened ascending branch over the Maritime Continent, these results suggest a weaker coupling between the Indian and Pacific Walker cells during the last glacial than today.

6. Summary and conclusions

We explored the response of the Western Pacific Warm Pool (WPWP) to local forcing and remote processes in dependence of astronomical parameters and glacial-interglacial varying boundary conditions.

We find that obliquity-controlled variations in southern hemisphere extratropical climate and ocean conditions have a strong impact on the thermocline off PNG, likely via variations in the subduction and lateral advection of the South Pacific Tropical Water. Specifically, a warming of thermocline waters in the WPWP is attributed to a reduced subduction and advection of relatively cool waters from the subtropical Pacific along with a reduced export of warm waters from the tropical Pacific when obliquity is high.

Records of surface $\delta^{18}O_{SW}$, Ti/Ca and Nd/Ca imply that variations in the amount of precipitation above PNG and the ambient ocean are mainly related to precession with enhanced (decreased) precipitation when precession is high (low). An increase (decrease) in precipitation is most probably linked to an intensification (reduction) of the ITCZ, a southward (northward) shift in the mean position of the ITCZ, and/or to an intensification (reduction) of the Australian monsoon. On the basis of our data we cannot resolve whether obliquity-related variations present in the Ti/Ca and foraminiferal Nd/Ca records are related to variations in precipitation or other effects, such as lateral advection and diagenetic overprinting.

The thermocline depth in the WPWP is predominantly controlled by changes in the Pacific Walker circulation in response to varying glacial-interglacial boundary conditions. Our new results show a deep thermocline during the LGM in comparison to the last interglacial and present conditions. A compilation of available surface-thermocline ΔT records from the WPWP illustrates a dipole-like pattern of LGM thermocline depth anomalies with a thermocline shoaling in the northern, and a deepening in the southern WPWP. A comparison of the proxy compilation to the output of PMIP2 and PMIP3/CMIP5 LGM climate model simulations reveals that only one model, the MRI-CGCM3, is able to capture the asymmetric TCD anomaly pattern evidenced by the data. In MRI-CGCM3, the spatial pattern of LGM thermocline depth anomalies is to a large extent attributable to glacial wind-field anomalies and associated Sverdrup dynamics that are related to a contracted Pacific Walker circulation during the LGM with enhanced ascent over the western equatorial Pacific Ocean, and reduced convection over the Maritime Continent. In conjunction with a strengthened glacial Indian Walker circulation with enhanced ascent over the eastern equatorial Indian Ocean and a weakened ascending branch over the Maritime Continent, our results suggest a weaker coupling between the Indian and Pacific Walker cells during the LGM than today.

Acknowledgements

We thank the captain, crew, and the scientific shipboard party of expedition SO–228 and acknowledge technical assistance from Henning Kuhnert, Birgit Meyer-Schack, Vera Lukies and Ryan Bu. Discussions with Thomas Westerhold helped to improve parts of the manuscript. The sample material was stored and supplied by the GeoB Core Repository at the MARUM – Center for Marine Environmental Sciences, University of Bremen, Germany. XRF data were acquired at the XRF Core Scanner Lab at MARUM. We acknowledge the World Climate Research Programme's Working Group on Coupled Modeling, which is responsible for CMIP, and the climate modeling groups (listed in Supplementary Table S2) for producing and making available their model output. For CMIP the U.S. Department of Energy's Program for Climate Model Diagnosis and Intercomparison provides coordinating support and led development of software infrastructure in partnership with the Global Organization for Earth System Science Portals. The Laboratoire des Sciences du Climat et de l'Environnement (LSCE) is acknowledged for collecting and archiving the PMIP2 model data. The PMIP2 Data Archive is supported by CEA, CNRS and the Programme National d'Etude de la Dynamique du Climat (PNEDC). M.P. acknowledges support from the German PalMod initiative (BMBF). We thank two anonymous reviewers for their constructive comments, which helped to improve the quality of our manuscript. This work is funded by the DFG-Research Center / Cluster of Excellence "The Ocean in the Earth System" and the BMBF project 03G0228A (EISPAC). The data presented in this study are available on Pangaea (www.pangaea.de).

Appendix A. Supplementary data

Supplementary data to this article can be found online at https://doi.org/10.1016/j.quascirev.2018.10.030.

References

Allen, K.A., Hönisch, B., Eggins, S.M., Haynes, L.L., Rosenthal, Y., Yu, J., 2016. Trace element proxies for surface ocean conditions: a synthesis of culture calibrations with planktic foraminifera. Geochem. Cosmochim. Acta 193, 197–221. https://doi.org/10.1016/j.gca.2016.08.015.

Anand, P., Elderfield, H., Conte, M.H., 2003. Calibration of Mg/Ca thermometry in planktonic foraminifera from a sediment trap time series. Paleoceanography 18 (2). https://doi.org/10.1029/2002PA000846.

Andreasen, D.J., Ravelo, A.C., 1997. Tropical Pacific Ocean thermocline depth reconstructions for the last glacial maximum. Paleoceanography 12 (3), 395–413. https://doi.org/10.1029/97PA00822.

Arbuszewski, J., deMenocal, P., Kaplan, A., Farmer, E.C., 2010. On the fidelity of shell-derived δ^{18}Oseawater estimates. Earth Planet Sci. Lett. 300 (3–4), 185–196. https://doi.org/10.1016/j.epsl.2010.10.035.

As-syakur, A.R., Adnyana, I.W.S., Mahendra, M.S., Arthana, I.W., Merit, I.N., Kasa, I.W., Ekayanti, N.W., Nuarsa, I.W., Sunarta, I.N., 2014. Observation of spatial patterns on the rainfall response to ENSO and IOD over Indonesia using TRMM Multi-satellite Precipitation Analysis (TMPA). Int. J. Climatol. 34 (15), 3825–3839. https://doi.org/10.1002/joc.393.

Aurahs, R., Treis, Y., Darling, K., Kucera, M., 2011. A revised taxonomic and phylogenetic concept for the planktonic foraminifer species *Globigerinoides ruber* based on molecular and morphometric evidence. Mar. Micropaleontol. 79 (1–2), 1–14. https://doi.org/10.1016/j.marmicro.2010.12.001.

Barker, S., Greaves, M., Elderfield, H., 2003. A study of cleaning procedures used for foraminiferal Mg/Ca paleothermometry. G-cubed 4 (9). https://doi.org/10.1029/2003GC000559.

Beaufort, L., de Garidel-Thoron, T., Mix, A.C., Pisias, N.G., 2001. ENSO-like forcing on oceanic primary production during the Late Pleistocene. Science 293 (5539), 2440–2444. https://doi.org/10.1126/science.293.5539.2440.

Beck, C., Grieser, J., Rudolf, B., 2005. A New Monthly Precipitation Climatology for the Global Land Areas for the Period 1951 to 2000. DWD, Klimastatusbericht KSB, 2004.

Bemis, B.E., Spero, H.J., Bijma, J., Lea, D.W., 1998. Reevaluation of the oxygen isotopic composition of planktonic foraminifera: experimental results and revised paleotemperature equations. Paleoceanography 13 (2), 150–160. https://doi.org/10.1029/98pa00070.

Berger, W.H., Bonneau, M.C., Parker, F.L., 1982. Foraminifera on the deep-sea floor: lysocline and dissolution rate. Oceanol. Acta 5, 249–258.

Blaauw, M., Christen, J.A., 2011. Flexible paleoclimate age-depth models using an autoregressive gamma process. Bayesian Analysis 6, 457–474. https://doi.org/10.1214/11-ba618.

Bolliet, T., Holbourn, A., Kuhnt, W., Laj, C., Kissel, C., Beaufort, L., Kienast, M., Andersen, N., Garbe-Schonberg, D., 2011. Mindanao dome variability over the last 160 kyr: episodic glacial cooling of the west pacific warm pool. Paleoceanography 26 (1). https://doi.org/10.1029/2010pa001966.

Bosmans, J.H.C., Hilgen, F.J., Tuenter, E., Lourens, L.J., 2015. Obliquity forcing of low-latitude climate. Clim. Past 11 (10), 1335–1346. https://doi.org/10.5194/cp-11-1335-2015.

Boyle, E.A., Keigwin, L.D., 1985. Comparison of Atlantic and Pacific paleochemical records for the last 215,000 years: changes in deep ocean circulation and chemical inventories. Earth Planet Sci. Lett. 76, 135–150.

Braconnot, P., Harrison, S.P., Kageyama, M., Bartlein, P.J., Masson-Delmotte, V., Abe-Ouchi, A., Otto-Bliesner, B., Zhao, Y., 2012. Evaluation of climate models using palaeoclimatic data. Nat. Clim. Change 2 (6), 417–424. https://doi.org/10.1038/nclimate1456.

Braconnot, P., et al., 2007. Results of PMIP2 coupled simulations of the Mid-Holocene and Last Glacial Maximum – Part 1: experiments and large-scale features. Clim. Past 3, 261–277. https://doi.10.5194/cp-3-261-2007.

Carton, J.A., Giese, B.S., 2008. A reanalysis of ocean climate using simple ocean data assimilation (SODA). Mon. Weather Rev. 136, 2999–3017.

Cheng, H., Sinha, A., Wang, X., Cruz, F., Edwards, R., 2012. The global paleomonsoon as seen through speleothem records from asia and the americas. Clim. Dynam. 39 (5), 1045–1062. https://doi.org/10.1007/s00382-012-1363-7.

Conroy, J.L., Thompson, D.M., Cobb, K.M., Noone, D., Rea, S., Legrande, A.N., 2017. Spatiotemporal variability in the δ^{18}O-salinity relationship of seawater across the tropical Pacific Ocean. Paleoceanography. https://doi.org/10.1002/2016pa003073.

Cresswell, G.R., 2000. Coastal currents of northern Papua New Guinea, and the Sepik River outflow. Mar. Freshw. Res. 51 (6), 553. https://doi.org/10.1071/mf99135.

Dang, H., Kissel, C., Bassinot, F., 2015. Precessional changes in the western equatorial Pacific hydroclimate: a 240 kyr marine record from the Halmahera Sea, East Indonesia. G-cubed 16, 148–164. https://doi.org/10.1002/2014GC005550.

Dang, H., Jian, Z., Bassinot, F., Qiao, P., Cheng, X., 2012. Decoupled Holocene variability in surface and thermocline water temperatures of the Indo-Pacific Warm Pool. Geophys. Res. Lett. 39 (1). https://doi.org/10.1029/2011gl050154.

de Garidel-Thoron, T., Rosenthal, Y., Bassinot, F., Beaufort, L., 2005. Stable sea surface temperatures in the western Pacific warm pool over the past 1.75 million years. Nature 433 (7023), 294–298. https://doi.org/10.1038/nature03189.

de Garidel-Thoron, T., Rosenthal, Y., Beaufort, L., Bard, E., Sonzogni, C., Mix, A.C., 2007. A multiproxy assessment of the western equatorial Pacific hydrography during the last 30 kyr. Paleoceanography 22. https://doi.org/10.1029/2006PA001269.

DiNezio, P.N., Clement, A., Vecchi, G.A., Soden, B., Broccoli, A.J., Otto-Bliesner, B.L., Braconnot, P., 2011. The response of the Walker circulation to Last Glacial Maximum forcing: implications for detection in proxies. Paleoceanography 26 (3). https://doi.org/10.1029/2010PA002083.

Ding, X., Bassinot, F., Guichard, F., Fang, N.Q., 2013. Indonesian throughflow and monsoon activity records in the Timor Sea since the last glacial maximum. Marine Micropaleontol. 101, 115–126. https://doi.10.1016/j.marmicro.2013.02.003.

Fairbanks, R.G., Wiebe, P.H., Bé, A.W.H., 1980. Vertical distribution and isotopic composition of living planktonic foraminifera in the western North Atlantic. Science 207 (4426), 61–63. https://doi.org/10.1126/science.207.4426.61.

Ford, H.L., Ravelo, A.C., Polissar, P.J., 2015. Reduced El nino-southern oscillation during the last glacial maximum. Science 347 (6219), 255–258. https://doi.org/10.1126/science.1258437.

Fraser, N., Kuhnt, W., Holbourn, A., Bolliet, T., Andersen, N., Blanz, T., Beaufort, L., 2014. Precipitation variability within the west pacific warm pool over the past 120 ka: evidence from the davao gulf, southern Philippines. Paleoceanography 29 (11), 1094–1110. https://doi.org/10.1002/2013pa002599.

Gagan, M.K., Hendy, E.J., Haberle, S.G., Hantoro, W.S., 2004. Post-glacial evolution of the indo-pacific warm pool and El niño-southern oscillation. Quat. Int. 118–119, 127–143. https://doi.org/10.1016/s1040-6182(03)00134-4.

Gill, A.E., 1980. Some simple solutions for heat-induced tropical circulation. Q. J. R. Meteorol. Soc. 106, 447–462. https://10.1002/qj.49710644905.

Gordon, A.L., 1986. Interocean exchange of thermocline water. J. Geophys. Res. 91 (C4), 5037. https://10.1029/JC091iC04p05037.

Gray, W.R., Weldeab, S., Lea, D.W., Rosenthal, Y., Gruber, N., Donner, B., Fischer, G., 2018. The effects of temperature, salinity, and the carbonate system on Mg/Ca in Globigerinoides ruber (white): a global sediment trap calibration. Earth Planet Sci. Lett. 482, 607–620. https://10.1016/j.epsl.2017.11.026.

Grenier, M., Jeandel, C., Lacan, F., Vance, D., Venchiarutti, C., Cros, A., Cravatte, S., 2013. From the subtropics to the central equatorial Pacific Ocean: neodymium isotopic composition and rare earth element concentration variations. J. Geophys. Res.: Oceans 118 (2), 592–618. https://doi.org/10.1029/2012jc008239.

Harrison, D.E., Vecchi, G.A., 2001. El Niño and La Niña - equatorial Pacific thermocline depth and sea surface temperature anomalies, 1986-98. Geophys. Res. Lett. 28 (6), 1051–1054. https://doi.org/10.1029/1999GL011307.

Harrison, S.P., Bartlein, P.J., Izumi, K., Li, G., Annan, J., Hargreaves, J., Braconnot, P., Kageyama, M., 2015. Evaluation of CMIP5 palaeo-simulations to improve climate projections. Nat. Clim. Change 5, 735–743. https://doi.org/10.1038/nclimate2649.

Hollstein, M., Mohtadi, M., Rosenthal, Y., Moffa Sanchez, P., Oppo, D., Martínez-Méndez, G., Steinke, S., Hebbeln, D., 2017. Stable oxygen isotopes and Mg/Ca in planktic foraminifera from modern surface sediments of the Western Pacific Warm Pool: implications for thermocline reconstructions. Paleoceanography. https://10.1002/2017PA003122.

Hönisch, B., Allen, K.A., Lea, D.W., Spero, H.J., Eggins, S.M., Arbuszewski, J., deMenocal, P., Rosenthal, Y., Russell, A.D., Elderfield, H., 2013. The influence of salinity on Mg/Ca in planktic foraminifers – evidence from cultures, core-top sediments and complementary δ^{18}O. Geochem. Cosmochim. Acta 121, 196–213. https://10.1016/j.gca.2013.07.028.

Hut, G., 1987. In: Consultants Group Meeting on Stable Isotopic Reference Samples for Geochemical and Hydrological Investigations. International Atomic Energy Agency, Vienna, p. 42.

Kawahata, H., Nishimura, A., Gagan, M.K., 2002. Seasonal change in foraminiferal production in the western equatorial Pacific warm pool: evidence from sediment trap experiments. Deep-Sea Res. Part II Top. Stud. Oceanogr. 49 (13–14), 2783–2800. https://doi.org/10.1016/S0967-0645(02)00058-9.

Kısakürek, B., Eisenhauer, A., Böhm, F., Garbe-Schönberg, D., Erez, J., 2008. Controls on shell Mg/Ca and Sr/Ca in cultured planktonic foraminiferan, *Globigerinoides ruber* (white). Earth Planet Sci. Lett. 273 (3–4), 260–269. https://doi.org/10.1016/j.epsl.2008.06.026.

Kissel, C., Laj, C., Kienast, M., Bolliet, T., Holbourn, A., Hill, P., Kuhnt, W., Braconnot, P., 2010. Monsoon variability and deep oceanic circulation in the western equatorial Pacific over the last climatic cycle: insights from sedimentary magnetic properties and sortable silt. Paleoceanography 25 (3). https://10.1029/2010pa001980.

Koutavas, A., Lynch-Stieglitz, J., Marchitto, T.M., Sachs, J.P., 2002. El Nino-like pattern in ice age tropical Pacific sea surface temperature. Science 297, 226–230.

Kuroda, Y., 2000. Variability of currents off the northern coast of New Guinea. J. Oceanogr. 56, 103–116. https://doi.org/10.1023/A:1011122810354.

Kutzbach, J.E., Liu, X., Liu, Z.Y., Chen, G., 2008. Simulation of the evolutionary response of global summer monsoons to orbital forcing over the past 280,000 years. Clim. Dynam. 360, 567–579. https://doi.org/10.1007/s00382-007-0308-z.

Laskar, J., 1990. The chaotic motion of the solar system: a numerical estimate of the size of the chaotic zones. Icarus 88, 266–291.

Lea, D.W., Pak, D.K., Spero, H.J., 2000. Climate impact of late quaternary equatorial pacific sea surface temperature variations. Science 289 (5485), 1719–1724.

Lee, S.Y., Poulsen, C.J., 2005. Tropical Pacific climate response to obliquity forcing in

the Pleistocene. Paleoceanography 20 (4). https://doi.org/10.1029/2005PA001161.
Leech, P.J., Lynch-Stieglitz, J., Zhang, R., 2013. Western pacific thermocline structure and the pacific marine intertropical convergence Zone during the last glacial maximum. Earth Planet Sci. Lett. 363, 133–143. https://doi.org/10.1016/j.epsl.2012.12.026.
Lisiecki, L.E., Raymo, M.E., 2005. A Pliocene-Pleistocene stack of 57 globally distributed benthic $\delta^{18}O$ records. Paleoceanography 20 (1). https://doi.org/10.1029/2004pa001071.
Liu, Y., et al., 2015. Obliquity pacing of the western pacific intertropical convergence Zone over the past 282,000 years. Nat. Commun. 6, 10018. https://doi.org/10.1038/ncomms10018.
Locarnini, R.A., et al., 2013. World Ocean Atlas 2013, Volume 1: Temperature. U.S. Government Printing Office, Washington, D.C.
Mantsis, D.F., Clement, A.C., Broccoli, A.J., Erb, M.P., 2011. Climate feedbacks in response to changes in obliquity. J. Clim. 24 (11), 2830–2845. https://doi.org/10.1175/2010jcli3986.1.
Mantsis, D.F., Lintner, B.R., Broccoli, A.J., Erb, M.P., Clement, A.C., Park, H.-S., 2014. The response of large-scale circulation to obliquity-induced changes in meridional heating gradients. J. Clim. 27 (14), 5504–5516. https://doi.org/10.1175/jcli-d-13-00526.1.
Martin, P.A., Lea, D.W., 2002. A simple evaluation of cleaning procedures on fossil benthic foraminiferal Mg/Ca. G-cubed 3 (10), 1–8. https://doi.org/10.1029/2001gc000280.
Martínez-Botí, M.A., Vance, D., Mortyn, P.G., 2009. Nd/Ca ratios in plankton-towed and core top foraminifera: confirmation of the water column acquisition of Nd. G-cubed 10 (8). https://doi.org/10.1029/2009gc002701.
McGregor, H.V., Gagan, M.K., McCulloch, M.T., Hodge, E., Mortimer, G., 2008. Mid-Holocene variability in the marine ^{14}C reservoir age for northern coastal Papua New Guinea. Quat. Geochronol. 3, 213–225. https://doi.org/10.1016/j.quageo.2007.11.002.
Merlis, T.M., Schneider, T., Bordoni, S., Eisenman, I., 2013. The tropical precipitation response to orbital precession. J. Clim. 26 (6), 2010–2021. https://doi.org/10.1175/jcli-d-12-00186.1.
Meyers, S.R., 2014. In: Astrochron: an R Package for Astrochronology. http://cran.r-project.org/packaeg=astrochron.
Mohtadi, M., Prange, M., Steinke, S., 2016. Palaeoclimatic insights into forcing and response of monsoon rainfall. Nature 533 (7602), 191–199. https://doi.org/10.1038/nature17450.
Mohtadi, M., Prange, M., Schefuß, E., Jennerjahn, T.C., 2017. Late Holocene slowdown of the Indian Ocean walker circulation. Nat. Commun. 8 (1). https://doi.org/10.1038/s41467-017-00855-3.
Mohtadi, M., Prange, M., Oppo, D.W., De Pol-Holz, R., Merkel, U., Zhang, X., Steinke, S., Luckge, A., 2014. North atlantic forcing of tropical Indian Ocean climate. Nature 509 (7498), 76–80. https://doi.org/10.1038/nature13196.
Mohtadi, M., et al., 2013. Report and Preliminary Results of RV SONNE Cruise SO-228, Kaohsiung-townsville, 04.05.2013- 23.06.2013, EISPAC-WESTWIND-SIODP, vol. 295. Berichte aus dem MARUM und dem Fachbereich Geowissenschaften der Universität Bremen, p. 110 urn:nbn:de:gbv:46-00103343-13.
Patrick, A., Thunell, R.C., 1997. Tropical Pacific sea surface temperatures and upper water column thermal structure during the Last Glacial Maximum. Paleoceanography 12 (5), 649–657. https://doi.org/10.1029/97pa01553.
Prange, M., Steph, S., Schulz, M., Keigwin, L.D., 2010. Inferring moisture transport across Central America: can modern analogs of climate variability help reconcile paleosalinity records? Quat. Sci. Rev. 29 (11–12), 1317–1321. https://10.1016/j.quascirev.2010.02.029.
Qu, T., Gao, S., Fine, R.A., 2013. Subduction of South Pacific Tropical Water and its equatorward pathways as shown by a simulated passive tracer. J. Phys. Oceanogr. 43 (8), 1551–1565. https://doi.org/10.1175/jpo-d-12-0180.1.
Rachmayani, R., Prange, M., Schulz, M., 2016. Intra-interglacial climate variability: model simulations of Marine Isotope Stages 1, 5, 11, 13, and 15. Clim. Past 12 (3), 677–695. https://doi.org/10.5194/cp-12-677-2016.
Radenac, M.-H., Rodier, M., 1996. Nitrate and chlorophyll distributions in relation to thermohaline and current structures in the western tropical Pacific during 1985-1989, *Deep Sea Research Part II*. Topical Studies in Oceanography 4–6, 725–752.
Radenac, M.H., Leger, F., Messie, M., Dutrieux, P., Menkes, C., Eldin, G., 2016. Wind-driven changes of surface current, temperature, and chlorophyll observed by satellites north of New Guinea. J Geophys Res-Oceans 121 (4), 2231–2252. https://doi.org/10.1002/2015JC011438.
Regoli, F., de Garidel-Thoron, T., Tachikawa, K., Jian, Z., Ye, L., Droxler, A.W., Lenoir, G., Crucifix, M., Barbarin, N., Beaufort, L., 2015. Progressive shoaling of the equatorial Pacific thermocline over the last eight glacial periods. Paleoceanography 30 (5), 439–455. https://doi.org/10.1002/2014pa002696.
Reimer, P.J., et al., 2013. IntCal13 and Marine13 radiocarbon age calibration curves 0–50,000 Years cal BP. Radiocarbon 55 (4), 1869–1887. https://doi.org/10.2458/azu_js_rc.55.16947.
Roberts, N.L., Piotrowski, A.M., Elderfield, H., Eglinton, T.I., Lomas, M.W., 2012. Rare earth element association with foraminifera. Geochem. Cosmochim. Acta 94, 57–71. https://doi.org/10.1016/j.gca.2012.07.009.
Rosenthal, Y., Boyle, E.A., Slowey, N., 1997. Temperature control on the incorporation of magnesium, strontium, fluorine, and cadmium into benthic foraminiferal shells from Little Bahama Bank: prospects for thermocline paleoceanography. Geochem. Cosmochim. Acta 61 (17), 3633–3643. https://doi.org/10.1016/S0016-7037(97)00181-6.
Rosenthal, Y., Field, M.P., Sherrell, R.M., 1999. Precise determination of element/calcium ratios in calcareous samples using sector field inductively coupled plasma mass spectrometry. Anal. Chem. 71 (15), 3248–3253. https://doi.org/10.1021/AC981410x.
Rosenthal, Y., Linsley, B.K., Oppo, D.W., 2013. Pacific Ocean heat content during the past 10,000 years. Science 342 (6158), 617–621. https://doi.org/10.1126/science.1240837.
Rosenthal, Y., Kalansky, J., Morley, A., Linsley, B.K., 2017. A paleo-perspective on ocean heat content: lessons from the Holocene and Common Era. Quat. Sci. Rev. 155, 1–12. https://doi.org/10.1016/j.quascirev.2016.10.017.
Rosenthal, Y., et al., 2004. Interlaboratory comparison study of Mg/Ca and Sr/Ca measurements in planktonic foraminifera for paleoceanographic research. G-cubed 5. https://10.1029/2003GC000650.
Russell, A.D., Hönisch, B., Spero, H.J., Lea, D.W., 2004. Effects of seawater carbonate ion concentration and temperature on shell U, Mg, and Sr in cultured planktonic foraminifera. Geochem. Cosmochim. Acta 68 (21), 4347–4361. https://doi.org/10.1016/j.gca.2004.03.013.
Sadekov, A.Y., Ganeshram, R., Pichevin, L., Berdin, R., McClymont, E., Elderfield, H., Tudhope, A.W., 2013. Palaeoclimate reconstructions reveal a strong link between El Nino-Southern Oscillation and Tropical Pacific mean state. Nat. Commun. 4, 2692. https://doi.org/10.1038/ncomms3692.
Sagawa, T., Yokoyama, Y., Ikehara, M., Kuwae, M., 2012. Shoaling of the western equatorial Pacific thermocline during the last glacial maximum inferred from multispecies temperature reconstruction of planktonic foraminifera. Palaeogeogr. Palaeoclimatol. Palaeoecol. 346–347, 120–129. https://doi.org/10.1016/j.palaeo.2012.06.002.
Sanchez Goñi, M.F., Harrison, S.P., 2010. Millennial-scale climate variability and vegetation changes during the Last Glacial: concepts and terminology. Quat. Sci. Rev. 29 (21–22), 2823–2827. https://doi.org/10.1016/j.quascirev.2009.11.014.
Schlitzer, R., 2014. In: odvawide (Ed.), Ocean Data View.
Schulz, M., Mudelsee, M., 2002. REDFIT: estimatingred-noise spectra directly from unevenly spaced paleoclimatic time series. Comput. Geosci. 28, 421–426.
Sholkovitz, E.R., Elderfield, H., Szymczak, R., Casey, K., 1999. Island weathering: river sources of rare earth elements to the Western Pacific Ocean. Mar. Chem. 68, 39–57.
Smith, I., Moise, A., Inape, K., Murphy, B., Colman, R., Power, S., Chung, C., 2013. ENSO-related rainfall changes over the New Guinea region. J. Geophys. Res.: Atmosphere 118 (19), 10,665-610,675. https://10.1002/jgrd.50818.
Soden, B.J., Held, I.M., 2006. An assessment of climate feedbacks in coupled ocean-atmosphere models. J. Clim. 19, 3354–3360. https://doi.org/10.1175/JCLI3799.1.
Steinke, S., Mohtadi, M., Groeneveld, J., Lin, L.-C., Löwemark, L., Chen, M.-T., Rendle-Bühring, R., 2010. Reconstructing the southern south China sea upper water column structure since the last glacial maximum: implications for the east asian winter monsoon development. Paleoceanography 25 (2). https://doi.org/10.1029/2009pa001850.
Tachikawa, K., Toyofuku, T., Basile-Doelsch, I., Delhaye, T., 2013. Microscale neodymium distribution in sedimentary planktonic foraminiferal tests and associated mineral phases. Geochem. Cosmochim. Acta 100, 11–23. https://10.1016/j.gca.2012.10.01.
Tachikawa, K., Timmermann, A., Vidal, L., Sonzogni, C., Timm, O.E., 2014. CO_2 radiative forcing and Intertropical Convergence Zone influences on western Pacific warm pool climate over the past 400 ka. Quat. Sci. Rev. 86 (0), 24–34. https://doi.org/10.1016/j.quascirev.2013.12.018.
Tachikawa, K., Cartapanis, O., Vidal, L., Beaufort, L., Barlyaeva, T., Bard, E., 2011. The precession phase of hydrological variability in the Western Pacific Warm Pool during the past 400 ka. Quat. Sci. Rev. 30 (25–26), 3716–3727. https://doi.org/10.1016/j.quascirev.2011.09.016.
Timmermann, A., Friedrich, T., Timm, O.E., Chikamoto, M.O., Abe-Ouchi, A., Ganopolski, A., 2014. Modeling obliquity and CO_2 effects on southern hemisphere climate during the Past 408 ka. J. Clim. 27 (5), 1863–1875. https://doi.org/10.1175/jcli-d-13-00311.1.
Tomczak, M., Godfrey, J.S., 2003. Regional Oceanography: an Introduction. Daya Publishing House, 391 pp.
Tsuchiya, M., Lukas, R., Fine, R., 1989. Source waters of the pacific equatorial undercurrent. Prog. Oceanogr. 23, 46.
Vecchi, G.A., Soden, B.J., Wittenberg, A.T., Held, I.M., Leetmaa, A., Harrison, M.J., 2006. Weakening of tropical Pacific atmospheric circulation due to anthropogenic forcing. Nature 441 (7089), 73–76. https://doi.org/10.1038/nature04744.
Waelbroeck, C., Labeyrie, L., Michel, E., Duplessy, J.C., McManus, J.F., Lambeck, K., Balbon, E., Labracherie, M., 2002. Sea-level and deep water temperature changes derived from benthic foraminifera isotopic records. Quat. Sci. Rev. 21 (1–3), 295–305. https://doi.org/10.1016/S0277-3791(01)00101-9.
Xu, J., Holbourn, A., Kuhnt, W., Jian, Z., Kawamura, H., 2008. Changes in the thermocline structure of the Indonesian outflow during Terminations I and II. Earth Planet Sci. Lett. 273 (1–2), 152–162. https://doi.org/10.1016/j.epsl.2008.06.029.
Xu, J.A., Kuhnt, W., Holbourn, A., Regenberg, M., Andersen, N., 2010. Indo-Pacific warm pool variability during the Holocene and last glacial maximum. Paleoceanography 25 (4), PA4230. https://10.1029/2010PA001934.
Yamasaki, M., Sasaki, A., Oda, M., Domitsu, H., 2008. Western equatorial Pacific planktic foraminiferal fluxes and assemblages during a La Niña year (1999). Mar. Micropaleontol. 66 (3–4), 304–319. https://doi.org/10.1016/j.marmicro.2007.10.006.

Zhang, P., Zuraida, R., Rosenthal, Y., Holbourn, A., Kuhnt, W., Xu, J., 2018. Geochemical characteristics from tests of four modern planktonic foraminiferal species in the Indonesian Throughflow region and their implications. Geoscience Frontiers. https://10.1016/j.gsf.2018.01.011.

Zhu, J., et al., 2017. Reduced ENSO variability at the LGM revealed by an isotope-enabled earth system model. Geophys. Res. Lett. https://doi.org/10.1002/2017gl073406.

Zweng, M.M., et al., 2013. World Ocean Atlas 2013, Volume 2: Salinity, Washington, D.C.